日本磁気学会
ISSN 2432-0250
Journal of the Magnetics Society of Japan
Electronic Journal URL: https://www.jstage.jst.go.jp/browse/msjmag

Vol.41 No.3　2017

Journal

JOURNAL OF THE MAGNETICS SOCIETY OF JAPAN

Vol.41 No.3 2017

日本磁気学会

ISSN 2432-0250

HP: http://www.magnetics.jp/ e-mail: msj@bj.wakwak.com

Electronic Journal: http://www.jstage.jst.go.jp/browse/msjmag

有限要素法解析ソフトウェア COMSOL Multiphysics®

COMSOL MULTIPHYSICS®

マルチフィジックスの進化論

無制限・強連成で実現象に即したシミュレーション事例のご紹介

永久磁石を利用した磁気軸受の解析例

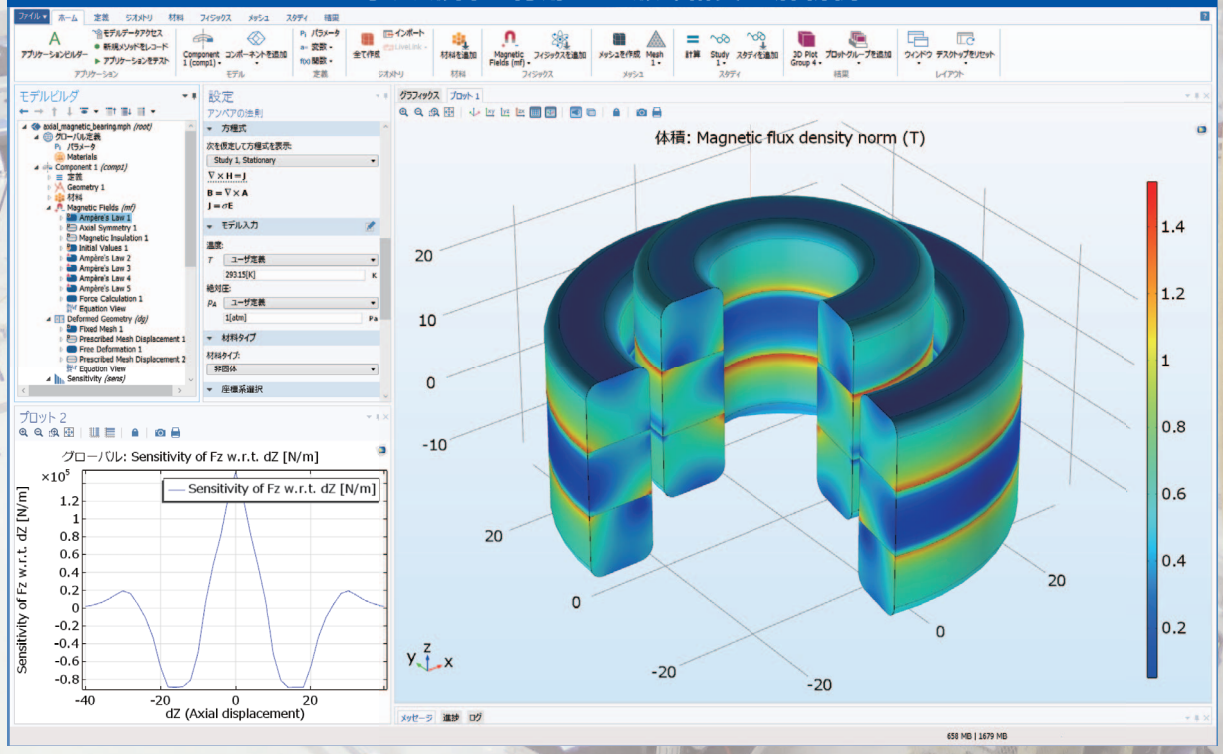

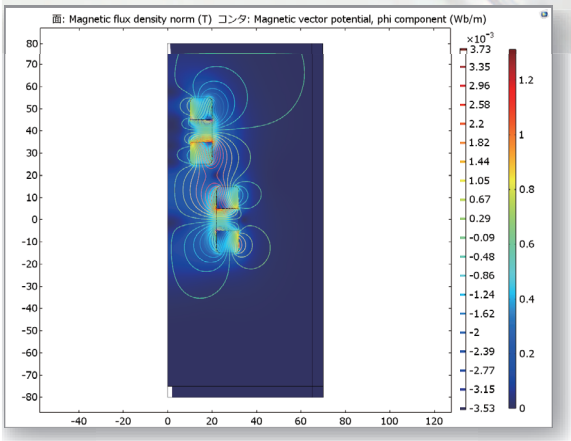

永久磁石を使用した磁気軸受

永久磁石を使用した軸受はターボ機械、ポンプ、モータ、発電機やフライホイール式エネルギー貯蔵システムなど、様々な分野で使用されています。非接触かつ潤滑不要で保守整備を大幅に省略できる点は、従来の機械式ベアリングと比べて重要なメリットです。
この例では、軸方向の永久磁石軸受の磁気力と剛性などの設計パラメータを計算する方法を示しています。

※AC/DCモジュールはCOMSOL Multiphysicsと併用するアドオン製品です。

AC/DC モジュールの適用例

- AC/DC 電流分布、電場分布
- バイオヒーティング
- コイルとソレノイド
- SPICE 回路とフィールドシミュレーション
- 接触抵抗
- 電磁両立性 (EMC) および電磁妨害 (EMI)
- 電磁力およびトルク
- 電磁力シールド
- 電気機械の変形
- ホール効果を利用したセンサ
- インシュレータ、コンデンサ、誘電体
- モータ、ジェネレータ、および他の電気機械
- 非線形材料
- 寄生容量とインダクタンス
- 永久磁石と電磁石
- 多孔質材料
- 抵抗および誘導加熱
- センサ
- 超伝導体
- 変圧器とインダクタ

COMSOL Multiphysics® なら、今まで不可能だった 3 種以上のマルチフィジックス解析を強連成で実現できます。30 日間全機能無料トライアル、無料の導入セミナー、1000種を超える世界の様々な事例をご提供いたします。詳しくは、下記の弊社営業部までお問い合せください。

COMSOL

http://www.comsol.jp

KESCO KEISOKU ENGINEERING SYSTEM
計測エンジニアリングシステム株式会社
http://www.kesco.co.jp/comsol/
Tel : 03-5282-7040 ・ Fax : 03-5282-0808

新製品

磁区観察ユニット

既存のプローバ装置で磁区観察を！
小型でシンプル！磁区観察をより手軽に！

※概要・特徴

- プローバ装置などに取り付けることが可能な小型・低価格の磁区観察ユニット
- 面内 / 垂直どちらの磁化方向にも対応
- 社内設計光学系による面内磁区の高コントラスト観察（空間分解能 3μm 以下 ）
- 光学系ヘッドの大きさは、 150×150×300mm 重量も 2kg と軽量・コンパクト
- 白色 LED 光源を用いた高安定性・長寿命
- オプションとして顕微鏡スタンド・ステージ・高機能観察 / 解析ソフトウェアなどを用意

※観察例

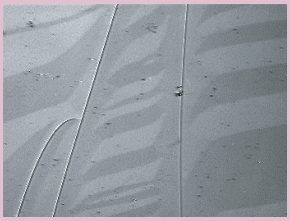

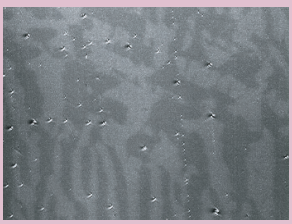

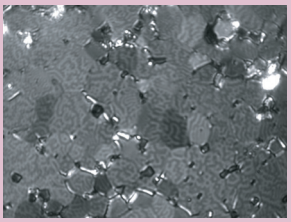

※オプション例

- θ-X-Y-Z 軸ステージ
- 顕微鏡スタンド

※この組み合わせでも重量は約 9kg ですので、 設置場所を選びません

この製品以外に、 30 年の研究現場への対応経験に基づいた高精度・高性能の磁気 Kerr 効果装置、Faraday 装置、 磁区観察顕微鏡など、 各種磁気光学製品の取り揃えがございます。
お気軽にお問合せください。

レーザとレーザ応用システム製品の総合メーカー
NEOARK ネオアーク株式会社
営 業 部／〒156-0041 東京都世田谷区大原2-17-6-108 TEL(03)6379-5539 FAX(03)6379-5688
大阪支店／〒541-0056 大阪市中央区久太郎町2-3-8-201 TEL(06)6271-5123 FAX(06)6271-5110
本社 第1工場･第2工場／八王子市
URL http://www.neoark.co.jp E-mail:info@neoark.co.jp

Physicist
Peter Grünberg

未来をどこまで想像できるか。

進みつづける時間の先に、何を見るか。
止まることのない時間の向こうに、何を思い描くか。
想像したことのない未来は、創造できない。
まっすぐな視線の先にしか、新しい常識は現れない。
先駆的なアイデアだって、革新的なテクノロジーだって、
それは、未来を自由に想像し、未来を強く渇望し、
そこに向かおうとするひたむきな意志からしか生まれない。
未来とは、前を向く者だけに与えられる、
現在という時間からのかけがえのない贈り物だ。
だから、未来に夢を見よう。未来に絵を描こう。
この世界の未来を、どこまでも想像しよう。

www.attractingtomorrow.tdk.co.jp

Attracting Tomorrow TDK

INDEX

世界初！
高温超電導型VSM

新製品

世界初*、高温超電導マグネットをVSMに採用することで
測定速度 当社従来機1/20を実現。
0.5mm cube磁石のBr, HcJ高精度測定が可能と
なりました。
*2014年7月 東英工業調べ

測定結果例

高温超電導VSMによるNdFeB(sint.) 0.5mm cube BHカーブ

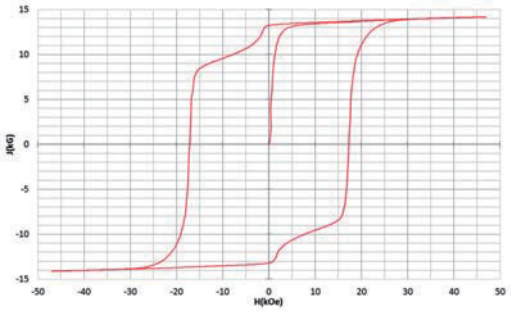

磁化測定レンジ：0.2emu
Br = 13.2kG　　HcJ = 17.2kOe

高温超電導VSMによるNdFeB(sint.) 1mm cube BHカーブ

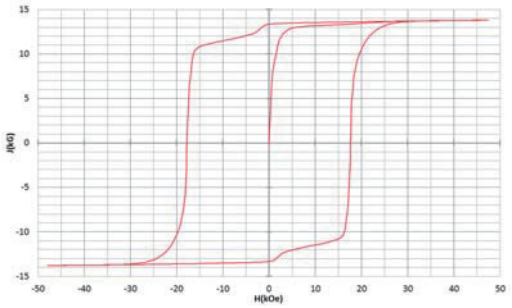

磁化測定レンジ：2emu
Br = 13.3kG　　HcJ = 17.7kOe

高温超電導VSMによるNdFeB(sint.) 4mm cube BHカーブ

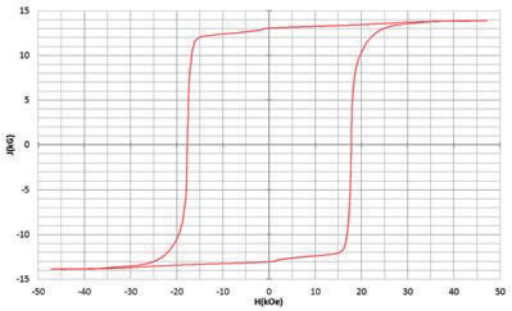

磁化測定レンジ：100emu
Br = 13.1kG　　HcJ = 17.8kOe

高速測定を実現

高温超電導マグネット採用により、高速測定を実現しました。Hmax= 5Tesla, Full Loop 測定が2分で可能です。
（当社従来機：Full Loop測定　40分）

小試料のBr,HcJ高精度測定

0.5mm cube 磁石のBr,HcJ 高精度測定ができ、表面改質領域を切り出しBr,HcJの強度分布等、微小変化量の比較測定が可能です。
また、試料の加工劣化の比較測定が可能です。

試料温度可変測定

－50℃～＋200℃温度可変UNIT（オプション）

磁界発生部の小型化

マグネットシステム部寸法：0.8m×0.3m×0.3m

TOEI 東英工業株式会社
http://www.toeikogyo.co.jp

〒194-0035 東京都町田市忠生1-8-13
TEL：042-791-1211　FAX：042-792-0490
E-mail : sales@toeikogyo.co.jp

Journal of the Magnetics Society of Japan
Vol. 41, No. 3

Electronic Journal URL: https://www.jstage.jst.go.jp/browse/msjmag

CONTENTS

J. Magn. Soc. Jpn., **41**, 46-51 (2017)

<Review>

Control of Magnetization Dynamics in Ordered Alloy Systems

T. Seki[*,**,***], W. Zhou[*], T. Yamamoto[*], and K. Takanashi[*,***]

[*]Institute for Materials Research, Tohoku University, *Sendai 980-8577, Japan*

[**]PRESTO, Japan Science and Technology Agency, *Saitama 322-0012, Japan*

[***]Center for Spintronics Research Network, Tohoku University, *Sendai 980-8577, Japan*

$L1_0$-type alloys and $L2_1$-type Heusler alloys are key materials for future spintronic and magnetic storage devices. $L1_0$-FePt with high uniaxial magnetic anisotropy is a promising material for ultrahigh density recording because of its high thermal stability of magnetization at a nanometer scale. Co-based Heusler alloys showing high spin polarization of conduction electrons enable us to enhance the magnetoresistance effect. In addition, utilizing the magnetization dynamics in these ordered alloys provides us with new paths in the development of spintronic and magnetic storage devices. In this review, we introduce the control of magnetization switching field for $L1_0$-FePt exchange-coupled with $Ni_{81}Fe_{19}$ by utilizing the spin waves in the bilayers, which will be useful for information writing. A nanometer-scaled rf oscillator is also introduced, in which the magnetization dynamics is excited by spin angular momentum transfer. We can improve both the rf output power and the oscillation quality simultaneously by using $Co_2(Fe_{0.4}Mn_{0.6})Si$ Heusler alloy.

Key words: $L1_0$-type ordered alloy, Heusler alloy, magnetization dynamics,

1. Introduction

We introduce our study on "Control of Magnetization Dynamics in Ordered Alloy Systems" in this review paper, which was a research subject of MSJ Outstanding Research Award 2016.

Rapid progress in electronic devices enables us to access various information everywhere, and the accessibility to a large amount of information makes our life comfortable and convenient. Among many kinds of electronic devices, magnetic and spintronic devices play significant roles in data storage technologies. Those devices exploit the direction of magnetization in a small magnet as an information bit, leading to the non-volatile data storage without external power supply. Since ultrahigh density data storage technologies are essential to manage "Big Data", one has highly desired the further development in spintronic and magnetic storage devices. In particular, it is important to simultaneously achieve ultrahigh density storage and ultralow power consumption for the device operation.

In addition to the existing data storage devices mentioned above, various spin-related phenomena have provided new concepts for the development of spintronic devices. For example, magnetization dynamics induced by the torque due to spin angular momentum transfer, which is called spin torque, have recently been found and demonstrated in nano-scaled devices [1]. That has opened a way to give novel functionalities to spintronic devices. From the viewpoint of practical applications, however, the significant improvement of device performance is still required.

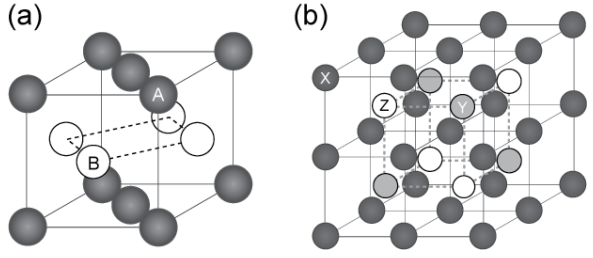

Fig. 1 Schematic illustrations of crystal structures for (a) $L1_0$-ordered and (b) $L2_1$-ordered alloys.

This review paper is devoted to two research subjects: one is the simultaneous achievement of ultrahigh density storage and ultralow power consumption for device operation. The other is the improvement of performance for spin torque devices, especially for a spin torque oscillator (STO) [2]. Key materials for the above research subjects are $L1_0$-type alloys and $L2_1$-type Heusler alloys (Fig. 1), both of which are ordered alloys. In addition to the ordered alloys, the magnetization dynamics is crucial to solve the issues for the magnetic storage and spintronic devices.

2. Spin-wave-assisted magnetization switching in exchange-coupled systems having $L1_0$-FePt

Spintronic and magnetic storage devices face a serious challenge in trying to simultaneously achieve ultrahigh density storage and ultralow power consumption for operation. In order to increase the storage density, the reduction of magnetic bit size is inevitable. A small magnetic volume (V) gives rise to the instability of magnetic information due to the thermal energy (k_BT, k_B is Boltzmann constant and T is temperature). Using a material with high magnetic anisotropy (K) is one of the possible solutions for this problem. However, the high K material leads to another problem, which is the significant increase in the external energy required for the information writing, *i.e.* magnetization switching. This is a dilemma that all the magnetic storage devices possess. A straightforward way to solve this dilemma is

that the switching field of a high K material is reduced only when one needs to switch its magnetization.

$L1_0$-ordered FePt ($L1_0$-FePt) alloy [3] is a representative of high K material, which exhibits the uniaxial magnetic anisotropy (K_u) of 7×10^6 J/m^3 along the c-axis of face-centered tetragonal. Thanks to this high K_u, $L1_0$-FePt is a candidate material for future ultrahigh density magnetic recording media [4]. As discussed above, however, its high K_u also gives rise to the large magnetization switching field (H_{sw}). If the magnetization switching occurs through the coherent rotation of magnetization [5], H_{sw} becomes equal to anisotropy field (H_{ani}). H_{ani} is given by $2\ K_u / M_s$, where M_s is the saturation magnetization. H_{sw} is roughly estimated to be larger than 100 kOe for fully $L1_0$-ordered FePt. Thus, a method to efficiently reduce H_{sw} for $L1_0$-FePt only during the information writing is needed.

A promising method for the efficient H_{sw} reduction is magnetization switching assisted by "external energy" such as microwave energy or thermal energy that are called microwave-assisted switching (MAS) [6,7] and heat-assisted switching [8]. In the case of MAS, microwave is applied to a magnet in order to excite its uniform magnetization precession mode, resulting in the amplification of precession angle followed by the magnetization switching at a low magnetic field. Although this MAS effectively reduces H_{sw}, the excitation frequency for MAS will become close to the sub-THz in case of high K materials such as $L1_0$-FePt because the uniform magnetization precession frequency is proportional to the effective field (H_{eff}) including H_{ani}. From the practical point of view, this high frequency required for MAS is an obstacle to design device structures. Instead of uniform magnetization precession mode, we utilize spin wave modes for an exchange-coupled bilayer system. In the following, we introduce "spin-wave-assisted magnetization switching method" [9-12], which enables us to effectively reduce H_{sw} for $L1_0$-ordered FePt by exciting the spin wave modes in a soft magnetic $Ni_{81}Fe_{19}$ (Permalloy, Py).

Figures 2(a) and 2(b) schematically illustrate the magnetic structures in the exchange-coupled bilayer consisting of the hard magnetic $L1_0$-FePt layer and the soft magnetic Py layer. The $L1_0$-FePt and Py layers are exchange-coupled at the interface, resulting in the magnetic structure where all the magnetic moments are aligned in the same direction. We call this saturated state. When small external magnetic field (H) was applied in the direction opposite to the magnetization vectors, the magnetic moments in Py easily start to rotate because of its low H_{sw}. However, the magnetic moments of Py around the interface are pinned by those of $L1_0$-FePt. As a result, a spatially twisted magnetic structure is formed in the exchange-coupled bilayer, which we call twisted state. In order to experimentally form this twisted magnetic structure, we prepared a

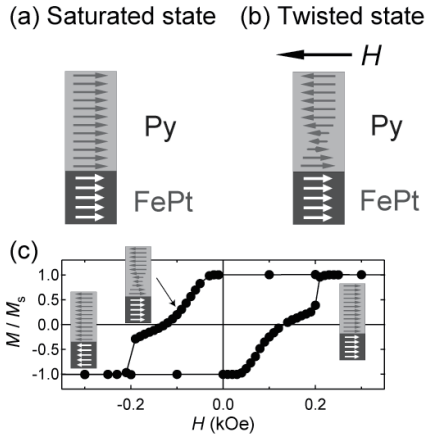

Fig. 2 Schematic illustrations of magnetic structures at (a) saturated state and (b) twisted state for the exchange-coupled bilayer consisting of the hard magnetic $L1_0$-FePt layer and the soft magnetic Py layer. (c) Magnetization curve for the $L1_0$-FePt | Py bilayer under the application of in-plane H [Ref. 11] together with magnetic structures.

thin film on an MgO (110) single crystal substrate using sputtering technique. The stacking of the thin film was MgO Subs. | | Fe (2) | Au (80) | FePt (10) | Py (100) | Au (3) (in nanometer). The FePt layer was grown on the Au buffer at 400 ºC. The substrate heating at 400 ºC promoted the formation of $L1_0$ ordered structure for the FePt layer, leading to the in-plane uniaxial magnetic anisotropy along the in-plane [001] direction. The magnetization curve for the $L1_0$-FePt | Py bilayer is shown in Fig. 2(c) [11], where the magnetization (M) was normalized by the saturated value of M (M_s) and H was applied along the in-plane [001] direction of $L1_0$-FePt. The gradual decrease in M was observed at the low H region. In this H region, the magnetization reversal process was reversible and the spring-back behavior appeared when the minor magnetization curve was measured. This reversible change indicates that the $L1_0$-FePt and the Py are exchange-coupled at the interface and the spatially twisted magnetic structure is formed in the bilayer by applying H.

The ferromagnetic resonance (FMR) spectra for the continuous film of the $L1_0$-FePt | Py bilayer are displayed in Fig. 3(a) [11]. The continuous film was put facedown onto the coplanar waveguide (CPW), and the vector network analyzer FMR technique was employed, where the frequency dependence of S_{11} (defined as the ratio of the reflected voltage to the input voltage) was measured. Three resonance peaks are observed both at H = 200 Oe and H = -200 Oe corresponding to the saturated state and the twisted state, respectively. These peak frequencies (f_0) are plotted as a function of H in Fig. 3(b) [11]. The open circles denote the experimental data whereas the solid curves are the

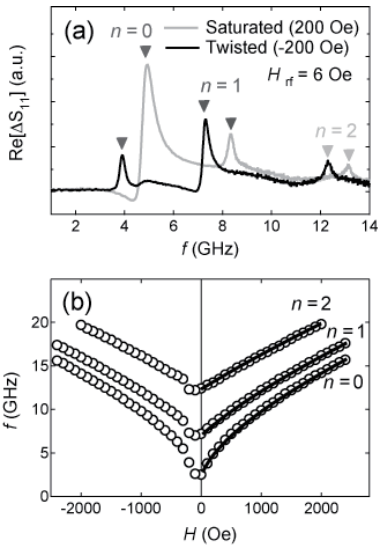

Fig. 3 (a) FMR spectra for the continuous film of the in-plane magnetized $L1_0$-FePt | Py bilayer measured at H = 200 Oe and -200 Oe, which correspond to the saturated and twisted states, respectively. (b) Peak frequencies as a function of H. The open circles denote the experimental data whereas the solid curves are the results of fitting based the analytical model of PSSW mode [Ref. 11].

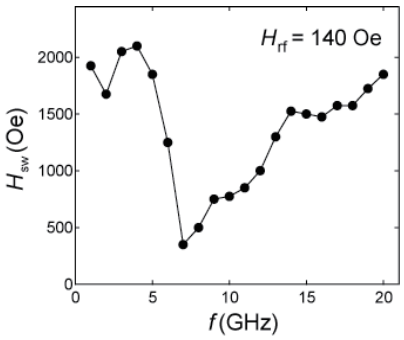

Fig. 4 H_{sw} as a function of excitation frequency for the device with the in-plane magnetized $L1_0$-FePt | Py bilayer. H_{rf} = 140 Oe was applied to the device [Ref. 11].

results of fitting based the analytical model of perpendicular standing spin wave (PSSW) mode [13]. The analytical model of PSSW well explained the dispersion relationship obtained experimentally. In addition to this fact, the numerical simulation suggested that the several PSSW modes with the different number of nodes (n) were mainly excited in the Py layer [9]. For example, n = 0 was the lowest order of the PSSW mode, in which the magnetic moments of Py were pinned at the interface with the hard magnetic $L1_0$-FePt whereas the magnetic moments of Py at the other interface showed the large-amplitude magnetization precession.

We examined the effect of the PSSW excitation on the magnitude of H_{sw} for the microfabricated $L1_0$-FePt | Py bilayer element. The continuous $L1_0$-FePt | Py bilayer was patterned into a rectangular element with dimensions of 2 μm × 50 μm by employing electron beam lithography and Ar ion milling. Figure 4 shows H_{sw} as a function of excitation frequency, where the rf magnetic field (H_{rf}) of 140 Oe was applied [11]. When H_{rf} was not applied, the device showed H_{sw} = 2350 Oe. Below f = 5.0 GHz, no remarkable change in H_{sw} occurred. However, the application of H_{rf} = 6 GHz reduced H_{sw} to 1250 Oe. The largest reduction was observed at f = 7 GHz, in which H_{sw} was obtained to be 350 Oe. This large H_{sw} reduction is attributable to the excitation of PSSW mode. As f was increased from 7 GHz to 20 GHz, H_{sw} increased monotonically. The monotonic increase of H_{sw} with f is the characteristic tendency for the spin wave-assisted switching, which is determined by the dispersion relationship of PSSW modes. In addition to the large H_{sw} reduction, this spin-wave-assisted magnetization switching showed the significant narrow H_{sw} distribution [11]. This narrowing in the H_{sw} distribution suggests that the resonantly amplified spin wave dynamics leads to the reduced H_{sw}. We also studied on the magnetization switching conditions under the spin wave excitation and revealed the limited region of switching condition [14]. This resonant switching behavior suggests that the spin-wave-assisted switching has potential for a selective switching technique in multilevel recording media.

In addition to the case of in-plane magnetized $L1_0$-FePt, we have recently investigated the magnetization dynamics of exchange-coupled bilayers with a perpendicularly magnetized $L1_0$-FePt, where the $L1_0$-FePt layer was epitaxially grown on an MgO (100) single crystal substrate with a Au buffer [12]. In order to examine the effect of magnetization dynamics of the exchange-coupled bilayer on H_{sw} for the perpendicularly magnetized $L1_0$-FePt, we exploited a nanodot consisting of the $L1_0$-FePt layers exchange-coupled with a soft magnetic Py layer having a magnetic vortex. The $L1_0$-FePt layer exhibited H_{sw} = 8.6 kOe without the H_{rf} application. When H_{rf} = 200 Oe with f = 11 GHz was applied, H_{sw} was reduced from 8.6 kOe to 2.8 kOe. By comparing the experimental result with the micromagnetic simulation, we found that the vortex dynamics of azimuthal spin waves in Py effectively triggered the reversed-domain nucleation in $L1_0$-FePt at a low H. This demonstrates that the excitation of spin wave leads to the efficient H_{sw} reduction even for the exchange-coupled system with the perpendicularly magnetized $L1_0$-FePt.

Although the excitation of spin wave dynamics in the exchange-coupled systems is useful to reduce H_{sw}, the present bilayer structures having the soft magnetic layer may lead to the degradation of thermal stability of magnetization compared with an $L1_0$-FePt single layer film. The evaluation of thermal stability for the

exchange-coupled bilayer will be an issue to be addressed in future.

3. Spin torque oscillator using Co-based Heusler alloy

Apart from the issue for ultrahigh density storage discussed in the previous Section, we also need to open up a way for new device applications for the further progress in the spintronics research field. In other words, we should provide spintronic devices with novel functionalities to realize a diversity of applications. An emerging spintronic device is STO [2], which is a nanometer-scaled rf oscillator, *e.g.* for on-chip communications or radar. The key physical phenomenon to operate the STO is the spin torque-induced magnetization dynamics. An STO consists of a layered structure of a ferromagnetic (F1) layer | a nonmagnetic (N) metal (or an insulator (I)) | another ferromagnetic (F2) layer. In case that we inject the electric current from F2 to F1, the conduction electrons are spin-polarized by the F1 layer (a spin polarizer), which exerts spin torque on the local magnetic moments of the F2 layer (a free layer). When the spin torque and the intrinsic damping torque are balanced in the F2 layer, the magnetization shows the self-sustained precession motion around H_{eff}. For current-perpendicular-to-plane (CPP) giant magnetoresistance (GMR) devices with F1 | N | F2 and magnetic tunnel junctions (MTJs) with F1 | I | F2, this steady magnetization precession produces a change in the device resistance via the GMR effect and the tunnel magnetoresistance effect, respectively [15-17]. Since a dc electric current (I_{dc}) is applied to the device, the time-dependent device resistance ($R(t)$) is converted into rf voltage (V_{rf}). Consequently, the device emits rf output power (P_{out}). This is the central mechanism of the STO, and its simple architecture composed of a single nanometer-scaled element is one of the attractive aspects of the STO.

However, the STOs have several crucial issues that need to be solved before the practical use: (i) the enhancement of P_{out}, (ii) improvement of the rf oscillation quality, and (iii) increasing the frequency tunability by an electric current and/or a magnetic field. MTJ-based STOs with an MgO tunnel barrier may solve the first issue since the P_{out} is roughly proportional to the square of the MR ratio. However, MTJ-based STOs have other problems, which are a wide oscillation linewidth observed generally [17], the risk of the dielectric breakdown of the tunnel barrier under large bias voltages [18], and the non-negligible shot noise due to the existence of tunnel barrier. On the other hand, a CPP-GMR device generally exhibits a narrow oscillation linewidth compared with the MTJ-based STOs [19]. Furthermore, a CPP-GMR stack is free from the risk of dielectric breakdown of a tunnel barrier material, and has the negligible contribution of shot noise. Thus, if the CPP-GMR effect can be enhanced, it could be a candidate of a high performance STO. One promising

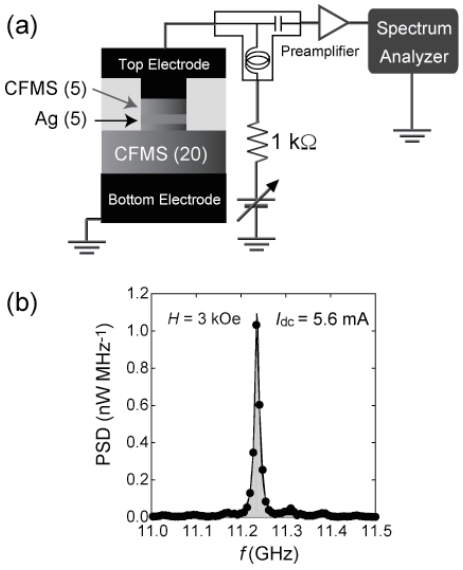

Fig. 5 (a) Schematic illustration of CPP-GMR device having CFMS | Ag | CFMS layers together with the measurement setup for rf oscillation properties, and (b) its rf spectrum at perpendicular H = 3 kOe and I_{dc} = 5.6 mA. The CPP nanopillar has an ellipsoidal shape of 0.1 × 0.17 μm^2. [Ref. 25]

way to enhance the MR ratio in a CPP-GMR device is to use half metallic ferromagnets showing the full spin-polarization of conduction electrons, in which the density of states at the Fermi level exists only in one spin channel.

Co_2MnSi (CMS) is one of the Co-based Heusler alloys theoretically predicted as a half metal [20] and showing high GMR ratio experimentally [21], leading to the enhancement of P_{out} even for a CPP-GMR-based STO. We reported that the large P_{out} = 1.1 nW was achieved for the CPP-GMR device with the CMS | Ag | CMS stack [22,23]. $Co_2Fe_{0.4}Mn_{0.6}Si$ (CFMS) is another full-Heusler alloy exhibiting high spin polarization of conduction electrons. In fact, the CPP-GMR devices with CFMS | Ag | CFMS showed the MR ratios larger than CMS | Ag | CMS [24]. Thus, CFMS is also a candidate material for developing high performance STO [25,26].

Figure 5(a) depicts a structure of the CPP-GMR having CFMS layers and the measurement setup to electrically detect the spin torque-induced magnetization dynamics. A stacking structure of Cr (20 nm) | Ag (40 nm) | CFMS (20 nm) | Ag (5 nm) | CFMS (3 nm) | Ag (2 nm) | Au (5 nm) was prepared on an MgO (100) single crystal substrate using an ultrahigh-vacuum magnetron sputtering system. The 20 nm-thick bottom CFMS and the 3 nm-thick top CFMS layers were grown at room temperature followed by *in-situ* annealing at 500ºC to promote the chemical ordering. The film was patterned into a CPP nanopillar with an ellipsoidal shape (0.1 × 0.17 μm^2). The top and the bottom CFMS layers for the

present device behave as the free layer and the fixed layer, respectively, against spin torque. The CPP-GMR device was connected to the circuit with a two-terminal rf probe and I_{dc} was applied through a bias-Tee. Positive I_{dc} is defined as the direction, in which electrons flow from the upper to the lower CFMS layer. The output V_{rf} was amplified by a preamplifier and was monitored in frequency-domain by a spectrum analyzer.

In order to understand the H direction dependence of oscillation properties, we measured the spin torque oscillation both under the in-plane and the perpendicular H. When in-plane H and I_{dc} were applied to the device along the long-axis of ellipsoidal pillar, the peak appeared in the power spectral density. However, the small P_{out} (0.03 nW) was obtained and a wide oscillation linewidth (Δf) of 76 MHz was observed, which were attributable to the inhomogeneous effective magnetic field (H_{eff}). In contrast to the spin torque oscillation under the in-plane H, we considerably improved the oscillation properties by applying the perpendicular H. Figure 5(b) displays an rf spectrum at

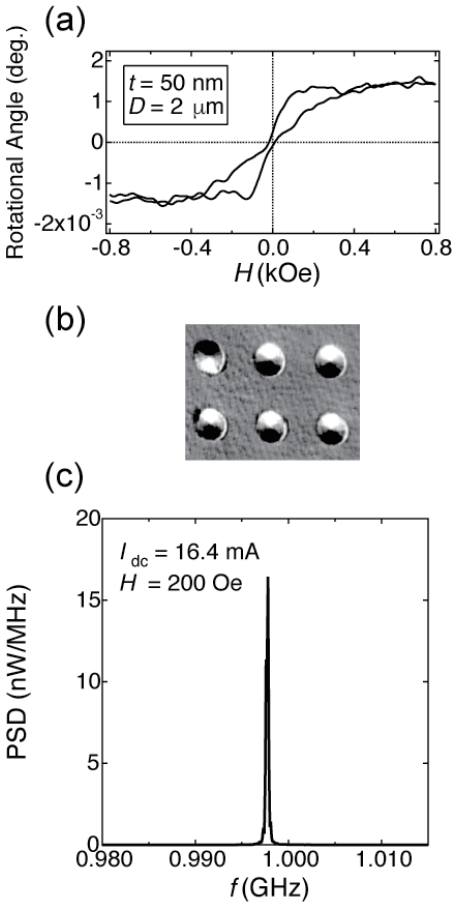

Fig. 6 (a) L-MOKE loop and (b) magnetic domain image at the remanence observed using PEEM-XMCD for the CFMS disks with the diameter of 2 μm and the thickness of 50 nm. [Ref. 28] (c) rf spectrum for the CPP-GMR device having the magnetic vortex in the CFMS layer.

H = 3 kOe and I_{dc} = 5.6 mA [25]. The I_{dc} dependence of oscillation frequency (f_0) showed the blue shift against I_{dc}, suggesting that the perpendicular H led to an out-of-plane mode of magnetization precession. The maximum value of P_{out} was obtained to be 23.7 nW together with the narrow Δf = 10 MHz. This P_{out} was much larger than those reported in the CPP-GMR devices using conventional ferromagnetic layers, and was one order of magnitude smaller than the performance of the previous MTJ-based STO showing P_{out} = 0.14 μW [17]. We also performed the micromagnetic simulation to reveal the detail of magnetization dynamics [25]. Although we successfully achieved the large P_{out} by using the highly spin-polarized CFMS, the simulated results suggested the formation of spatially non-uniform magnetic structure during the spin torque oscillation and the large incoherency in the precession trajectory. This implies that the improvement of coherency in the spin torque oscillation enables us to further enhance P_{out}.

One of the possible ways to improve the coherency of spin torque oscillation is to utilize the dynamics of magnetic vortex. A study on the vortex STO reported the narrow Δf, leading to the high Q factor (Δf / f_0) [27], which is owing to the stable vortex oscillation. The stability of vortex oscillation originates from the topologically stable magnetic structure and good consistency of the magnetization distribution with the spatial distribution of the Oersted field formed by the dc current. Thus, we examined the formation of magnetic vortex and the control of vortex dynamics in the CFMS nanodisk, in which the CFMS layers were epitaxially grown on the MgO substrate. Figures 6(a) and 6(b) show the longitudinal magneto-optical Kerr effect (L-MOKE) loop and the magnetic domain image at the remanence observed using a photoemission electron microscope with X-ray magnetic circular dichroism (PEEM-XMCD), respectively, for the circular CFMS disks with the diameter of 2 μm and the thickness of 50 nm [28]. The shape of L-MOKE loop with low remanent magnetization was attributed to the magnetization process undergoing the formation of magnetic vortex. In addition, the curling in-plane magnetic moments were clearly observed in the magnetic domain image. Consequently, one sees that the magnetic vortex can be stably formed even in the epitaxially grown CFMS disks. Then, we fabricated the STO with the CFMS disk with a diameter of 240 nm, in which the magnetic vortex was formed in the CFMS disk [29]. The STO was made of the stack of MgO (100) Subs. | | Cr (20 nm) | Ag (20 nm) | CFMS (20 nm) | Ag (5 nm) | CFMS (30 nm) | Ag (2 nm) | Au (3 nm), in which 30 nm-thick CFMS was patterned into the disk shape to stabilize the magnetic vortex. Figure 6(c) shows an rf spectrum for the CPP-GMR device having the magnetic vortex in the CFMS layer. The sub-GHz oscillation with a narrow oscillation linewidth (Δf = 0.4 MHz) was observed, which originated from the vortex dynamics. From the

systematic study on the oscillation properties for vortex STO with CFMS, we found that the high P_{out} > 10 nW and the high Q factor > 5000 were achieved simultaneously at an optimum condition [29]. Our experimental results indicate that the utilization of vortex dynamics in CFMS is a promising way to provide a significant improvement of the performance of STOs.

4. Summary

In this review, we introduced two research topics: spin-wave-assisted magnetization switching in the bilayers with $L1_0$-FePt and Py, and high performance STOs using the CFMS Heusler alloy.

For the in-plane and perpendicularly magnetized configurations of $L1_0$-FePt layers, we successfully reduced H_{sw} for $L1_0$-FePt utilizing the spin waves in the bilayers. We expect that this spin-wave-assisted magnetization switching will be used as an information writing technique of future magnetic storage devices.

The STOs having the CFMS layers were developed, and both the P_{out} and the Q factor were improved by exploiting the highly spin-polarization of CFMS Heusler alloy and the dynamics of magnetic vortex. We believe that vortex STO with CFMS serves as a key for the further progress in spintronic devices.

Acknowledgements These works are partly in collaboration with Dr. H. Imamura, Dr. H. Arai and Dr. T. Yamaji (AIST), Prof. Y. Nozaki (Keio Univ.), Prof. M. Mizuguchi, Prof. T. Kubota, Dr. H. Yako (Tohoku Univ.), Dr. Y. Sakuraba (NIMS), and Prof. M. Kotsugi (Tokyo Univ. of Sci.). We also thank Dr. T. Ohkochi (SPring-8) and Mr. Y. Murakami and Mr. I. Narita (Tohoku Univ.) for their technical assistance. These works were partially supported by a Grant-in-Aid for Young Scientists A (25709056), Grant-in-Aid for Scientific Research S (23226001), Grant-in-Aid for Scientific Research B (16H04487), Institute for Division For Interdisciplinary Advanced Research and Education, Tohoku Univ. and the Japan Society for the Promotion Science Research Fellowship for Young Scientist. The device fabrication and the structural characterization were partly performed at Cooperative Research and Development Center for Advanced Materials, IMR, Tohoku University.

References

1) Brataas, A. D. Kent, and H. Ohno: *Nature Mater.* 11, 372 (2012).
2) D. C. Ralph and M. D. Stiles: *J. Magn. Magn. Mater.* 320, 1190 (2008).
3) O. A. Ivanov, L. V. Solina, V. A. Demshina, and L. M. Magat: *Phys. Met. Metallogr.* 35, 81 (1973).
4) D. Weller, A. Moser, L. Folks, M. E. Best, W. Lee, M. F. Toney, M. Schwickert, J. U. Thiele, and M. F. Doerner. *IEEE Trans. Magn.* 36, 10 (2000)
5) E. C. Stoner and E. P. Wohlfarth: *Nature* 160**,** 650 (1947)
6) J.-G. Zhu, X. Zhu, and Y. Tang: *IEEE Trans. Magn.* 44, 125 (2008).
7) S. Okamoto, N. Kikuchi, M. Furuta, O. Kitakami, and T. Shimatsu: *J. Phys. D: Appl. Phys.* 48, 353001 (2015).
8) D. Atkinson and R. P. Cowburn: *Appl. Phys. Lett.* **85**, 1386 (2009).
9) T. Seki, K. Utsumiya, Y. Nozaki, H. Imamura, and K. Takanashi: *Nature Comm.,* 4, 1726 (2013).
10) T. Seki, K. Hotta, H. Imamura, Y. Nozaki, and K. Takanashi: *Appl. Phys. Lett.* 103, 122403 (2013).
11) T. Seki, W. Zhou, and K. Takanashi: *J. Phys. D: Appl. Phys.* 49, 075002 (2016).
12) W. Zhou, T. Seki, H. Arai, H. Imamura, and K. Takanashi: *Phys. Rev. B* 94, 220401(R) (2016).
13) S. O. Demokritov, B. Hillebrands, and A. N. Slavin: *Phys. Reports* 348, 441 (2001).
14) W. Zhou, T. Yamaji, T. Seki, H. Imamura, and K. Takanashi: *Appl. Phys. Lett.* (Accepted).
15) S. I. Kiselev, J. C. Sankey, I. N. Krivorotov, N. C. Emley, R. J. Schoelkopf, R. A. Buhrman, and D. C. Ralph: *Nature* 425, 380 (2003).
16) W. H. Rippard, M. R. Pufall, S. Kaka, S. E. Russek, and T. J. Silva: *Phys. Rev. Lett.* 92 027201 (2004).
17) A. M. Deac, A. Fukushima, H. Kubota, H. Maehara, Y. Suzuki, S. Yuasa, Y. Nagamine, K. Tsunekawa, D. D. Djayaprawira, and N. Watanabe: *Nature Phys.* 4, 803 (2008).
18) D. Houssameddine, S. H. Florez, J. A. Katine, J.-P. Michel, U. Ebels, D. Mauri, O. Ozatay, B. Delaet, B. Viala, L. Folks, B. D. Terris, and M.-C. Cyrille: *Appl. Phys. Lett.* 93, 022505 (2008).
19) Q. Mistral, J.-V. Kim, T. Devolder, P. Crozat, C. Chappert, J. A. Katine, M. J. Carey, and K. Ito: *Appl. Phys. Lett.* 88, 192507 (2006).
20) S. Ishida, S. Asano, and J. Ishida: *J. Phys. Soc. Jpn.*, 53, 2718 (1984).
21) Y. Sakuraba, K. Izumi, Y. Miura, K. Fuasukawa, T. Iwase, S. Bosu, K. Saito, K. Abe, M. Shirai, and K. Takanashi: *Phys. Rev. B* **82**, 094444 (2010).
22) R. Okura, Y. Sakuraba, T. Seki, K. Izumi, M. Mizuguchi, and K. Takanashi: *Appl. Phys. Lett.*, 99, 052510 (2011).
23) T. Seki, Y. Sakuraba, R. Okura, and K. Takanashi: *J. Appl. Phys.* 113, 033907 (2013).
24) Y. Sakuraba, M. Ueda, Y. Miura, K. Sato, S. Bosu, K. Saito, M. Shirai, T.J. Konno, and K. Takanashi: *Appl. Phys. Lett.* 101, 252408 (2012).
25) T. Seki, Y. Sakuraba, H. Arai, M. Ueda, R. Okura, H. Imamura, and K. Takanashi: *Appl. Phys. Lett.* 105, 092406 (2014).
26) T. Yamamoto, T. Seki, T. Kubota, H. Yako, and K. Takanashi: *Appl. Phys. Lett.* 106, 092406 (2015).
27) V. S. Pribiag, I. N. Krivorotov, G. D. Fuchs, P. M. Braganca, O. Ozatay, J. C. Sankey, D. C. Ralph, and R. A. Buhrman: *Nature Phys.* 3 498-503 (2007).
28) T. Yamamoto, T. Seki, M. Kotsugi, and K. Takanashi: *Appl. Phys. Lett.* 108, 152402 (2016).
29) T. Yamamoto, T. Seki, and K. Takanashi: *Phys. Rev. B* 94, 094419 (2016).

Received Feb. 08, 2017; Accepted Mar. 08, 2017

J. Magn. Soc. Jpn., **41**, 52-57 (2017)

<Paper>

Impact of Damping Constant on Bit Error Rate in Heat-Assisted Magnetic Recording

T. Kobayashi, Y. Nakatani*, F. Inukai, K. Enomoto, and Y. Fujiwara

Graduate School of Engineering, Mie Univ., *1577 Kurimamachiya-cho, Tsu 514-8507, Japan*

*Graduate School of Informatics and Engineering, Univ. of Electro-Communications, *1-5-1 Chofugaoka, Chofu 182-8585, Japan*

We calculate the writing field dependence of the bit error rate for Gilbert damping constants of 0.1 and 0.01 in heat-assisted magnetic recording (HAMR) using a new model calculation. The attempt period used in the new model calculation is considered in detail. The writing properties are examined for various thermal gradients, linear velocities, and anisotropy constants. When the damping constant is equal to 0.1, write-error is smaller, and erasure-after-write is larger than that for 0.01 since the attempt period is short. The physical implication of the results is discussed. We also compare the results of the new model calculation and the conventionally used micromagnetic calculation. The overall tendencies of the results are the same. Therefore, the outline of the impact of the damping constant on the bit error rate in HAMR can be understood by the grain magnetization reversal probability and the attempt period used in the new model calculation.

Key words: heat-assisted magnetic recording, damping constant, thermal gradient, linear velocity, anisotropy constant

1. Introduction

Heat-assisted magnetic recording (HAMR) is a promising candidate for high-density magnetic recording beyond the trilemma limit[1].

We have already proposed a new HAMR model calculation[2] using the grain magnetization reversal probability for each attempt. The new model calculation can obtain the bit error rate (bER) as a function of the writing field H_w for a given anisotropy constant ratio K_u/K_{bulk} [3]. We discussed the physical implication of the recording time window using the new model calculation. And then, we provided the allowable ranges of H_w and K_u/K_{bulk} for various Curie temperatures.

The grain magnetization reversal probability and the attempt period, whose inverse is the attempt frequency f_0, are key physical quantities in the new model calculation. The reversal probability is a function of the anisotropy field H_k, and H_k is a function of temperature. The temperature dependence of experimental H_k values can be represented by a mean field analysis[4]. On the other hand, the f_0 value is a function of the anisotropy constant K_u, and K_u is a function of temperature, and then f_0 at the writing temperature is necessary. Furthermore, f_0 is a function of the damping constant α [5], and α is also a function of temperature[6, 7]. Therefore, although knowledge of α at the writing temperature is necessary, it is unknown.

In this study, we calculate the f_0 value at the writing temperature employing the conventionally used micromagnetic calculation, and then we calculate the writing field dependence of the bER for α = 0.1 and 0.01 in HAMR using the new model calculation, and discuss the physical implication of the results for various thermal gradients, linear velocities, and anisotropy constants. We also compare the results with those obtained using the micromagnetic calculation.

2. Calculation Method

2.1 Calculation conditions

The medium was assumed to be granular. The calculation conditions are summarized in Table 1. Since we assume high-density magnetic recording such as 4 Tbpsi, we suppose the grain number per bit n and the bit pitch d_B to be 4 and 6.8 nm, respectively. The grain volume V_m for the mean grain size D_m is $D_m^2 \times h$ = 193 nm^3 where h is the grain height. The standard deviations of the grain size σ_D/D_m, the anisotropy constant, and the Curie temperature are assumed to be 10, 0, and 0 %, respectively.

Errors occur in some grains of a bit. We assume that if the area ΣD_i^2 of the grains where the magnetization turns in the recording direction is more than 50 % (signal threshold) of nD_m^2 in one bit, the bit is error-free. The bit error rates in this paper are useful only in a comparison.

The medium can be designated by the Curie temperature T_c = 700 K and the anisotropy constant ratio K_u/K_{bulk} = 0.4 or 0.8 where K_u/K_{bulk} is the intrinsic ratio of the medium anisotropy constant K_u to bulk FePt K_u [3].

Figure 1 shows schematic illustrations of the writing field switching timing and grain arrangement. Four grains are arranged in the cross-track direction. It is assumed that the thermal gradient is zero for the cross-track direction. H_w and $\tau_{min} = d_B/v$ are the writing field and the minimum magnetization transition window, respectively, where v is the linear velocity. There are fluctuations of switching timing $\Delta\tau$ and position Δx in a granular medium as shown in Fig. 1 (a). However, we assume $\Delta\tau$ = 0 and Δx = 0

for our discussion of the intrinsic phenomenon as shown in Fig. 1 (b). The H_w direction (recording direction) is upward when $0 \le \tau \le \tau_{min}$ and downward otherwise. When the medium temperature T becomes T_c, the time τ is set at zero.

Table 1 Calculation conditions.

Grain number per bit n (grain / bit)	4
Bit pitch d_B (nm)	6.8
Mean grain size D_m (nm)	4.9
Grain height h (nm)	8
Standard deviation of grain size σ_D / D_m (%)	10
Signal threshold	0.5
Curie temperature T_c (K)	700
Anisotropy constant ratio K_u / K_{bulk}	0.4, 0.8

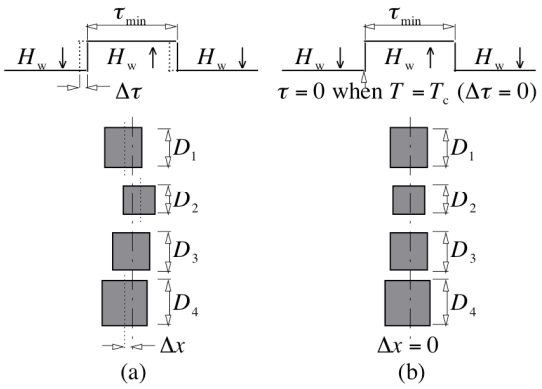

Fig. 1 Writing field switching timing and arrangement of grains for (a) a granular medium and (b) this model.

2.2 Model calculation

The grain magnetization reversal number N during τ is given by[1)]

$$N = f_0 \tau \exp\left(-K_\beta\right), \tag{1}$$

where f_0 and K_β are the attempt frequency and the medium thermal stability factor. When τ = 10 years, Eq. (1) is frequently used as a guideline for 10 years of archiving. And, when $\tau = 1/f_0 = \tau_{AP}$ (attempt period), Eq. (1) becomes

$$P = \exp\left(-K_\beta\right), \tag{2}$$

which can be used as a guideline for writing and for the grain magnetization reversal probability P for each attempt. This will be confirmed later employing the conventionally used micromagnetic calculation. $K_{\beta+}$ where the grain magnetization M_s is parallel to H_w, and $K_{\beta-}$ where M_s is antiparallel to H_w, are expressed by

$$K_{\beta+}(T, H_w) = \frac{K_u(T)V}{kT}\left(1 + \frac{H_w}{H_k(T)}\right)^2, \tag{3}$$

and

$$K_{\beta-}(T, H_w) = \frac{K_u(T)V}{kT}\left(1 - \frac{H_w}{H_k(T)}\right)^2 \quad \left(H_w \le H_k(T)\right),$$

$$K_{\beta-}(T, H_w) = 0 \quad \left(H_k(T) < H_w\right), \tag{4}$$

respectively, where K_u, V, k, and $H_k = 2K_u / M_s$ are the anisotropy constant, the grain volume, the Boltzmann constant, and the anisotropy field, respectively. The probability P_+ for each attempt where M_s and H_w change from parallel to antiparallel is expressed by

$$P_+ = \exp\left(-K_{\beta+}\right). \tag{5}$$

On the other hand,

$$P_- = \exp\left(-K_{\beta-}\right) \tag{6}$$

is the probability for each attempt where M_s and H_w change from antiparallel to parallel.

The key physical quantities in the new model calculation are $P_\pm$, f_0, and their temperature dependence. The temperature dependence of M_s was determined using a mean field analysis[3)], and that of K_u was assumed to be proportional to M_s^2. T_c can be adjusted by the Cu simple dilution of $(Fe_{0.5}Pt_{0.5})_{1-z}Cu_z$. $M_s(T_c, T)$ is a function of T_c and T, and $M_s(T_c = 770\ \mathrm{K}, T = 300\ \mathrm{K})$ = 1000 emu/cm^3 was assumed. On the other hand, $K_u(T_c, K_u / K_{bulk}, T)$ is a function of T_c, K_u / K_{bulk}, and T, and $K_u(T_c = 770\ \mathrm{K}, K_u / K_{bulk} = 1, T = 300\ \mathrm{K})$ = 70 Merg/cm^3 was assumed. $P_\pm$ is a function of H_k. If the Curie temperature is high, the temperature dependence of the experimental H_k values can be represented by a mean field analysis[3, 4)].

On the other hand, since f_0 is a function of K_u, and K_u is decreased by elevating the temperature during writing, we require f_0 at the writing temperature rather than that at room temperature. We calculate the f_0 value at the writing temperature with a micromagnetic calculation using the Landau-Lifshitz-Gilbert (LLG) equation[5)].

Furthermore, f_0 is a function of the Gilbert damping constant α[5)]. We have already presented the formula for the temperature dependence of α for ferrimagnetic materials[6)]. This was confirmed experimentally[7)]. The temperature dependence of α can also be expected for ferromagnetic materials used in HAMR. Although α at the writing temperature is necessary, it is unknown. Therefore, we deal with α = 0.1 and 0.01 in this paper.

The calculation procedure is described below. First, the medium is determined by T_c and K_u / K_{bulk}. The grain temperature falls from T_c according to the thermal gradient $\partial T / \partial x$ for the down-track direction and according to v during the writing process. The

magnetic property and then $P_{\pm}$ are calculated by employing a mean field analysis for each τ_{AP}. The magnetization direction can be determined by the Monte Carlo method for each τ_{AP}. The bit error rate (bER) is obtained from the mean value of 10^6 bits since the results are scattered. Then the bER can be calculated as a function of H_w [2].

2.3 Micromagnetic calculation

We carried out a micromagnetic calculation using the LLG equation and the temperature dependences of the magnetic properties used in the model calculation. The calculation conditions were also the same except that thirty-two grains were used in the cross-track direction instead of four to achieve a good signal-to- noise ratio (SNR). The writing field is assumed to be spatially uniform, the direction is perpendicular to the medium plane, and the rise time is zero. Both the demagnetizing and the magnetostatic fields are neglected during writing.

The output signal, media noise, and media SNR were calculated using a sensitivity function[8] of 218 nm, which is the same as the cross track width of the simulation region, a wide magnetoresistive read head with a 15 nm shield-shield spacing, and a 4.0 nm head-medium spacing.

3. Calculation Results

3.1 Attempt frequency

First, we calculate the attempt frequency f_0 for media where α = 1 and T_c = 700 K at T = 650 K for various K_u/K_{bulk} values. Figure 2 shows the grain volume V dependence of f_0. Since we use the values of V_m = 193 nm^3 and K_u/K_{bulk} = 0.4 or 0.8 in this paper, f_0 is about 4×10^{11} s^{-1} or 14×10^{11} s^{-1}, respectively. Since f_0 is proportional to $\alpha/(1+\alpha^2)$ [5], the $\tau_{AP}=1/f_0$ values used for α = 0.1 and 0.01 are 0.013 and 0.13 ns, respectively, when K_u/K_{bulk} = 0.4. If K_u/K_{bulk} = 0.8, τ_{AP} is 0.036 ns for α = 0.01.

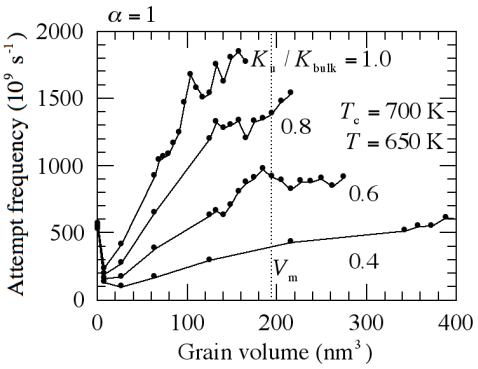

Fig. 2 Dependence of attempt frequency on grain volume for various anisotropy constant ratios K_u/K_{bulk}.

3.2 Thermal gradient

Next, we examine the dependence of the bER on H_w for various $\partial T/\partial x$ values when v = 10 m/s. Figure 3 (a) shows the result for α = 0.1. The decreasing bER as H_w increases from 0 to about 5 kOe is caused by a reduction of normal write-error (WE), and the bER that increases as H_w increases to more than about 5 kOe is caused by erasure-after-write (EAW)[2]. WE occurs during writing. On the other hand, EAW occurs after writing ($\tau_{min} \le \tau$), and the grain magnetization reverses in the opposite direction to the recording direction by changing the H_w direction at τ_{min}. No dependence of WE on $\partial T/\partial x$ is observed, and EAW can be suppressed by increasing $\partial T/\partial x$. This is explained using the time dependence of H_k as shown in Fig. 4 and the time dependence of P_- for each attempt as shown by filled circles in Fig. 5 (a). Since the increase rate of H_k with time becomes steep as $\partial T/\partial x$ increases as shown in Fig. 4, the decrease rate of P_- with time becomes steep as $\partial T/\partial x$ increases in Fig. 5 (a). The writing time is the duration from τ = 0 to a certain time where the P_- value is relatively high, for example 10^{-1} or 10^{-2}. The τ_{AP} value is only 0.013 ns and much shorter than the writing time. The attempt number of magnetization reversal N_{AN} during writing is sufficiently large regardless of the $\partial T/\partial x$ values. Therefore, no dependence of WE on $\partial T/\partial x$ is observed.

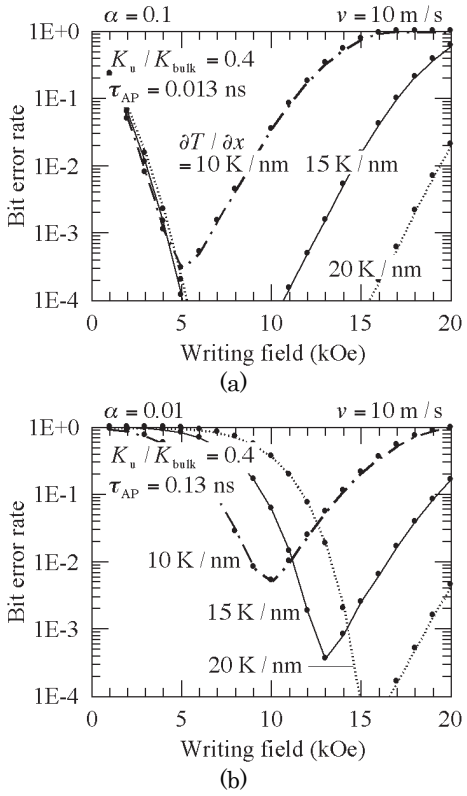

Fig. 3 Dependence of bit error rate (bER) on writing field H_w for various thermal gradients $\partial T/\partial x$ when linear velocity v = 10 m/s where (a) damping constant α = 0.1 and (b) 0.01.

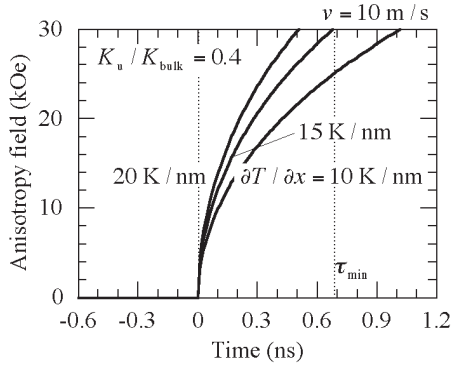

Fig. 4 Dependence of anisotropy field on time for various $\partial T/\partial x$ values.

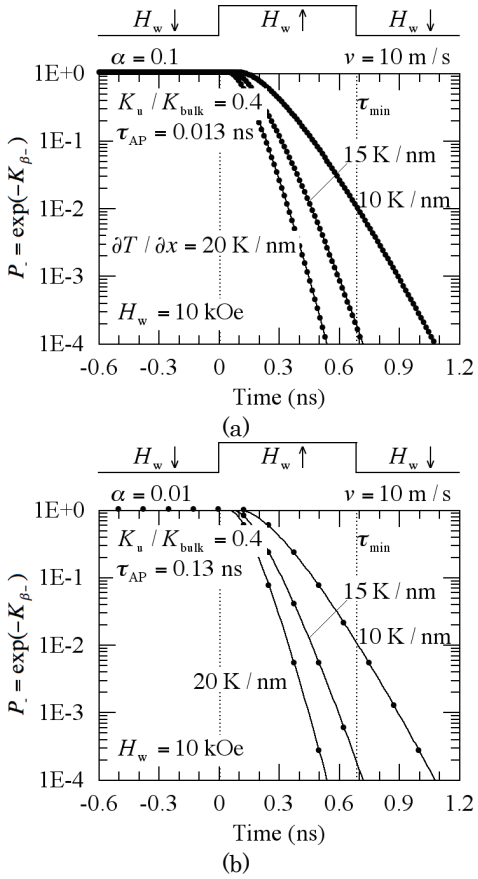

Fig. 5 Dependence of grain magnetization reversal probability P_- on time for various $\partial T/\partial x$ values where (a) α = 0.1 and (b) 0.01.

EAW is determined by P_- after τ_{min} and τ_{AP}. P_- after τ_{min} is decreased as $\partial T/\partial x$ increases as shown in Fig. 5 (a). Therefore, EAW can be suppressed by increasing $\partial T/\partial x$ as shown in Fig. 3 (a).

The dependence of the bER on H_w for α = 0.01 is shown in Fig. 3 (b). The dependence of WE on $\partial T/\partial x$ can be seen, and EAW can be suppressed by increasing $\partial T/\partial x$. This is also explained using the time dependence of P_- for each attempt as shown in Fig. 5 (b). Although the time dependences of P_- are the same in Figs. 5 (a) and (b), τ_{AP} for α = 0.01 is 0.13 ns and much longer than that for α = 0.1. Since N_{AN} during writing is very small, writing becomes difficult and a higher H_w is necessary[2]. Furthermore, since N_{AN} during writing depends on the $\partial T/\partial x$ values, the dependence of WE on $\partial T/\partial x$ can be seen.

Furthermore, EAW for α = 0.01 in Fig. 3 (b) becomes smaller than that for α = 0.1 in Fig. 3 (a) when compared at the same H_w value. Since N_{AN} after writing for α = 0.01 becomes much smaller than that for α = 0.1, EAW for α = 0.01 becomes small.

We also compared the results of the new model calculation and the conventionally used micromagnetic calculation. Figure 6 shows the dependence of the SNR on H_w, which is calculated with a micromagnetic simulation. Figures 6 (a) and (b) correspond to Figs. 3 (a) and (b), respectively. The bER value of 10^{-2} in Fig. 3 may be compared with the SNR value of zero or a few dB in Fig. 6. When α = 0.1 (Fig. 6 (a)), writing is possible in a low H_w, and the tendency of EAW in Fig. 6 (a) is the same as that in Fig 3 (a). On the other hand, when α = 0.01 (Fig. 6 (b)), the tendency for writing to be difficult in a low H_w is also the same as that in Fig. 3 (b).

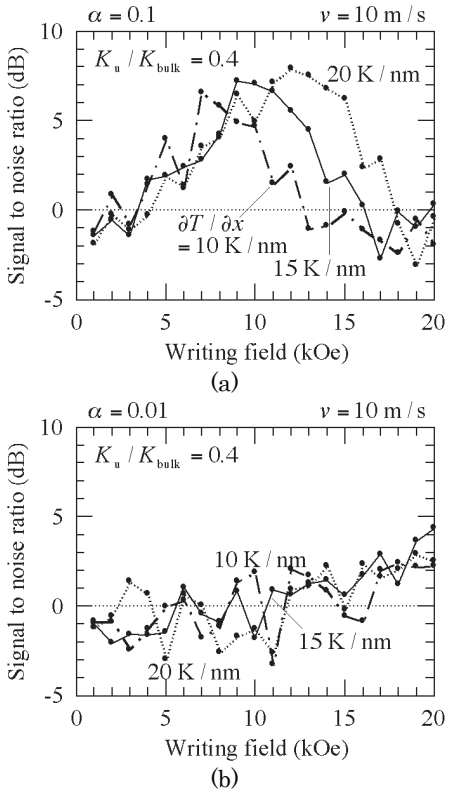

Fig. 6 Dependence of signal-to-noise ratio (SNR) on H_w for various $\partial T/\partial x$ values where (a) α = 0.1 and (b) 0.01.

3.3 Linear velocity

The dependence of bER on H_w for various v values when $\partial T/\partial x$ = 15 K/nm is also examined. Figure 7 (a) shows the result for α = 0.1. WE and EAW are almost independent of v. This is explained using the time dependence of P_- for each attempt as shown by the

filled circles in Fig. 8 (a). Since τ_{min} is d_B/v, τ_{min} changes and decreases with v. However, since d_B and $\partial T/\partial x$ are constant, the temperature at τ_{min}, that is $T_c - d_B \cdot \partial T/\partial x$, does not change with v. The P_- values at τ_{min} are the same regardless of the v values. In addition, τ_{AP} is very short, and N_{AN} during writing is sufficiently large regardless of the v values. Therefore, WE and EAW have almost no dependence on v.

The bER dependence on H_w for α = 0.01 is shown in Fig. 7 (b). The WE dependence on v can be seen, and is suppressed by decreasing v. This is also explained using the time dependence of P_- for each attempt as shown in Fig. 8 (b). Although N_{AN} is only two when $0 \le \tau < \tau_{min}$ for v = 20 m/s, it becomes ten for v = 5 m/s. Therefore, N_{AN} during writing is increased as v decreases, and WE can be suppressed by decreasing v. In other words, since τ_{AP} is long, it is effective to write slowly by reducing v on the reduction of WE.

Figure 9 shows the SNR dependence on H_w, which is calculated with a micromagnetic simulation. Figures 9 (a) and (b) correspond to Figs. 7 (a) and (b), respectively. When α = 0.1, the tendency of the bER value of 10^{-2} in Fig. 7 (a) is the same as that of the SNR value of zero or a few dB in Fig. 9 (a). Furthermore, when α = 0.01, the tendency for SNR to improve by decreasing v in Fig 9. (b) corresponds to the fact that WE decreases as v decreases in Fig. 7 (b).

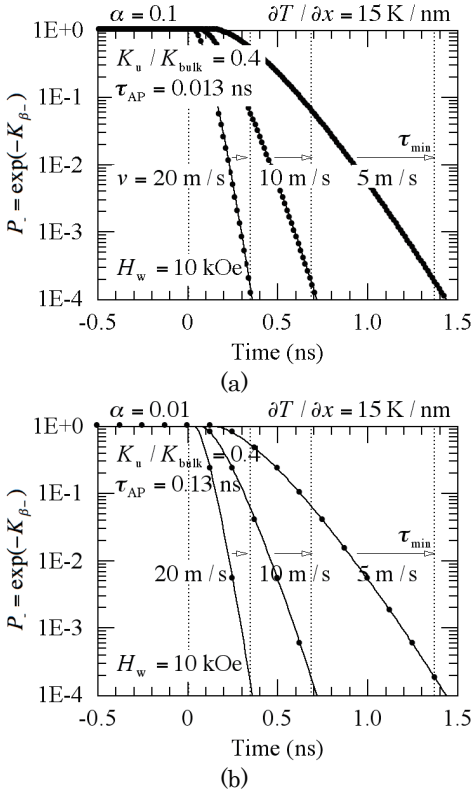

Fig. 8 Dependence of P_- of grain on time for various v values where (a) α = 0.1 and (b) 0.01.

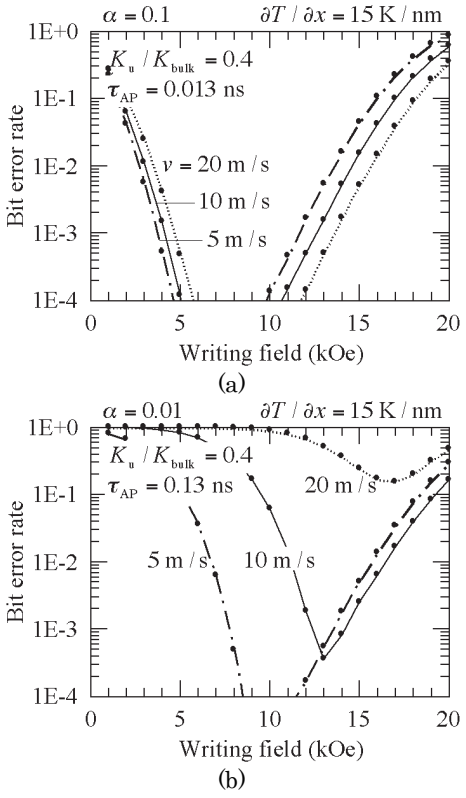

Fig. 7 Dependence of bER on H_w for various v values when $\partial T/\partial x$ = 15 K/nm where (a) α = 0.1 and (b) 0.01.

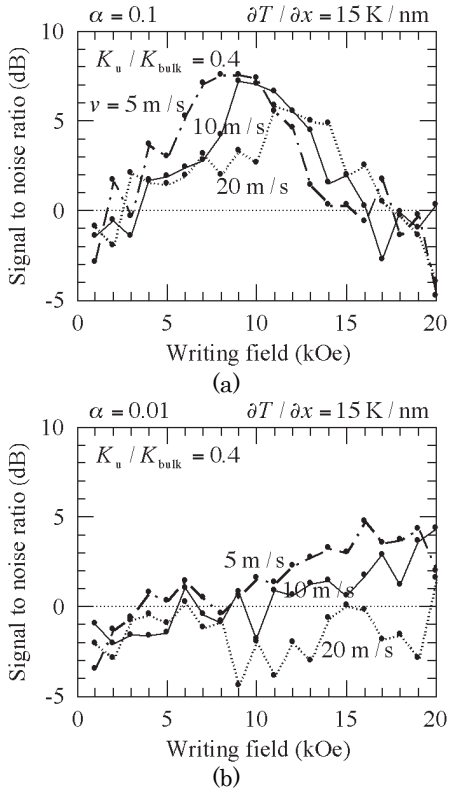

Fig. 9 Dependence of SNR on H_w for various v values where (a) α = 0.1 and (b) 0.01.

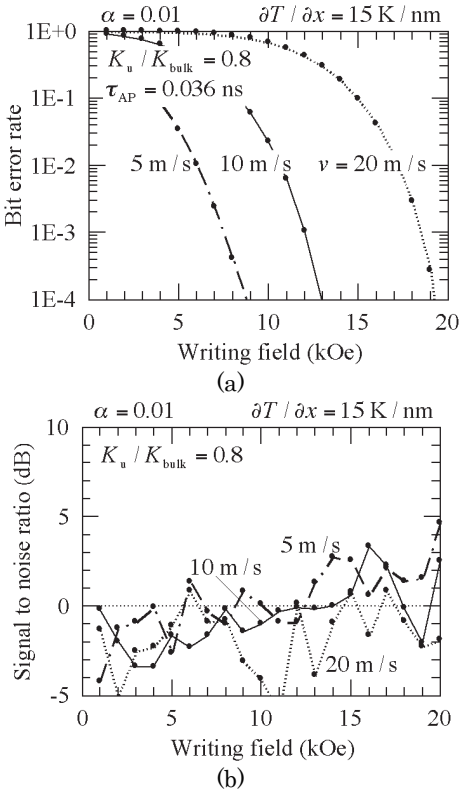

Fig. 10 (a) Dependence of bER and (b) dependence of SNR on H_w for α = 0.01 and K_u / K_{bulk} = 0.8.

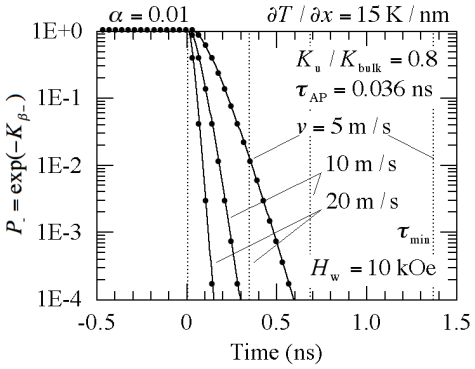

Fig. 11 Dependence of P_- of grain on time for α = 0.01 and K_u / K_{bulk} = 0.8.

3.4 Anisotropy constant

When α = 0.01, τ_{AP} is too long to write with a low H_w. Since f_0 can be increased, then τ_{AP} can be reduced by increasing K_u / K_{bulk} as shown in Fig. 2, we examine the writing properties for a high K_u / K_{bulk}.

Figure 10 shows (a) the dependence of bER and (b) the corresponding dependence of SNR on H_w for α = 0.01 and K_u / K_{bulk} = 0.8 instead of K_u / K_{bulk} = 0.4 in Fig. 7 (b) and Fig. 9 (b), respectively. The overall tendencies for WE are the same in Fig. 10 (a) and Fig. 7 (b). This can be explained using Fig. 11. The τ_{AP} value for α = 0.01 and K_u / K_{bulk} = 0.8 is 0.036 ns, which is decreased from 0.13 ns by increasing K_u / K_{bulk}. However, the reduction rate of P_- becomes steep by increasing K_u / K_{bulk} as shown in Fig. 11 in comparison with Fig. 8 (b). Therefore, the WE values are almost the same for K_u / K_{bulk} = 0.4 and 0.8.

A comparison of Fig. 10 (a) and Fig. 7 (b) shows that EAW is suppressed by increasing K_u / K_{bulk}. This can be understood clearly from the steep P_- decrease in Fig. 11.

4. Conclusions

We calculated the writing field dependence of the bit error rate (bER) for the Gilbert damping constants α = 0.1 and 0.01 in heat-assisted magnetic recording (HAMR) using a new model calculation.

When α = 0.1, write-error (WE) is smaller, and erasure-after-write (EAW) is larger than that for α = 0.01 since the attempt period τ_{AP} is short. EAW decreases as the thermal gradient increases.

When α = 0.01, writing becomes difficult and a high writing field is necessary since τ_{AP} is long. WE decreases as the thermal gradient or the linear velocity decreases.

EAW can be decreased by increasing the anisotropy constant.

We confirmed the results of the new model calculation by comparison with those of the conventionally used micromagnetic calculation. The overall tendencies were the same. Therefore, the outline of the impact of α on bER in HAMR can be understood by the grain magnetization reversal probability and the attempt period used in the new model calculation.

Acknowledgements We acknowledge the support of the Advanced Storage Research Consortium (ASRC), Japan.

References

1) S. H. Charap, P. -L. Lu, and Y. He: *IEEE Trans. Magn.*, **33**, 978 (1997).
2) T. Kobayashi, F. Inukai, K. Enomoto, and Y. Fujiwara: *J. Magn. Soc. Jpn.*, **41**, 1 (2017).
3) T. Kobayashi, Y. Isowaki, and Y. Fujiwara: *J. Magn. Soc. Jpn.*, **39**, 8 (2015).
4) T. Kobayashi, Y. Isowaki, and Y. Fujiwara: *J. Magn. Soc. Jpn.*, **40**, 28 (2016).
5) Y. Nakatani, Y. Uesaka, N. Hayashi, and H. Fukushima: *J. Magn. Magn. Mat.*, **168**, 347 (1997).
6) T. Kobayashi, H. Hayashi, Y. Fujiwara, and S. Shiomi: *IEEE Trans. Magn.*, **41**, 2848 (2005).
7) C. D. Stanciu, A. V. Kimel, F. Hansteen, A. Tsukamoto, A. Itoh, A. Kirilyuk, and Th. Rasing: *Phys. Rev. B*, **73**, 220402(R) (2006).
8) Y. Kanai, Y. Jinbo, T. Tsukamoto, S. J. Greaves, K. Yoshida, and H. Muraoka: *IEEE. Trans. Magn.*, **46**, 715 (2010).

Received Oct. 16, 2016; Revised Dec. 17, 2016; Accepted Mar. 8, 2017

J. Magn. Soc. Jpn., **41**, 58-62 (2017)

<Paper>

Morphology and magnetic properties of α"-$Fe_{16}N_2$ nanoparticles synthesized from iron hydroxide and iron oxides

M. Tobise, T. Ogawa, and S. Saito

Department of Electronic Engineering, Graduate School of Engineering, Tohoku University,

6–6–05, Aza–Aoba, Aramaki, Aoba–ku, Sendai 980–8579, Japan

Metastable α"-$Fe_{16}N_2$ have attracted much interest as a candidate for rare-earth-free hard magnetic materials. To realize high coercivity, it is necessary to utilize not only the magnetocrystalline anisotropy but also the shape anisotropy of α"-$Fe_{16}N_2$ nanoparticles assemblies. An increase in magnetostatic couplings and intergranular exchange couplings among particles typically reduces the coercivity. Therefore, it is very important to evaluate the anisotropy and magnetic interactions among α"-$Fe_{16}N_2$ nanoparticles. We have examined the changes in morphology, structure and magnetic properties through the synthesis of α"-$Fe_{16}N_2$ nanoparticles from various materials such as α-FeOOH, ɤ-Fe_2O_3, and Fe_3O_4. The magnetic interactions were also estimated based on experimental results obtained by analysis of the rotational hysteresis loss of randomly oriented nanoparticles. H_c and H_k^{ptc} for the α"-$Fe_{16}N_2$ nanoparticle assemblies for different starting materials ranged from 2.2 to 1.1 kOe, and from 11 to 12 kOe respectively. Experimental results of the normalized coercive force and normalized switching field suggests that the existence of large magnetic interactions among α"-$Fe_{16}N_2$ nanoparticles.

Key words: nanomagnetics, hard magnetic materials, iron nitride, magnetic anisotropy, rare earth element-free

1. Introduction

The metastable α"-$Fe_{16}N_2$ iron nitride phase with body-centered tetragonal (b.c.t.) structure has received much attention as a candidate for rare-earth-free hard magnetic materials. After a surprising first report where the α"-$Fe_{16}N_2$ phase exhibited giant saturation magnetization as a thin film[1], many researches have attempted to produce single phase α"-$Fe_{16}N_2$[2,3]. In 1993, a thin film method was established to achieve a relatively high volume fraction of α"-$Fe_{16}N_2$ using reactive sputtering, where a saturation magnetization of $M_s \simeq 240$ emu/g and uniaxial magnetocrystalline anisotropy constant of $K_u \simeq 1\times10^7$ erg/cm^3 were determined[4]. These values are very attractive with respect to the realization of a permanent magnet based on this material. Since it is still very difficult to produce metastable α"-$Fe_{16}N_2$ in thin films, the synthesis of single phase α"-$Fe_{16}N_2$ in bulk form is considered to be extremely challenging[5,6,7]. In 2013, a procedure for the synthesis of single phase α"-$Fe_{16}N_2$ nanoparticles was established, and α"-$Fe_{16}N_2$ was reported[8] to exhibit $M_s \simeq 226$ emu/g and $K_u \simeq 9.6\times10^6$ erg/cm^3 at 300 K.

To produce a hard magnetic material using magnetic particle, it is necessary to control the anisotropy of particle assemblies and the magnetic interaction among these particles. Magnetostatic couplings and intergranular exchange couplings among particles typically reduce the coercivity. Therefore it is very important to evaluate these magnetic interactions among α"-$Fe_{16}N_2$ nanoparticles. In this work, we examine the changes in the morphology, structure and magnetic properties of α"-$Fe_{16}N_2$ nanoparticles synthesized using different starting materials, such as α-FeOOH, ɤ-Fe_2O_3, and Fe_3O_4. We also discuss the magnetic anisotropy and magnetic interactions based on the experimental results obtained by the rotational hysteresis loss analysis[9] of randomly oriented nanoparticles.

2. Experimental Procedure

The synthesis of α"-$Fe_{16}N_2$ nanoparticles was conducted using commercially available α-FeOOH (Wako Pure Chemical Industries, Ltd.), ɤ-Fe_2O_3 (CIK NanoTek Corporation) and Fe_3O_4 (Mitsui Mining & Smelting Co., Ltd.). The diameters of the iron hydroxide and iron oxide particles ranged from several tens to several hundreds of nanometers. The temperature and duration for reduction and nitriding were systematically examined to obtain almost single phase α"-$Fe_{16}N_2$, according to the following procedure. α-FeOOH, ɤ-Fe_2O_3, and Fe_3O_4 nanoparticles were first reduced at 250−600 °C for 1−5 h in a H_2 gas flow. Nitriding was subsequently performed at 100−200 °C for 2−72 h in an NH_3 gas flow. Crystal structure analysis was conducted using powder X-ray diffraction (XRD) with CoKα radiation. Morphological changes were observed using transmission electron microscopy (TEM). For magnetic properties measurements, α-Fe and α"-$Fe_{16}N_2$ nanoparticles were packed into a disk shape (6 mm diameter, 1 mm thick) with resin. The magnetization σ, and coercivity H_c, were measured using vibrating sample magnetometer (VSM) with a maximum applied magnetic field of 14.5 kOe at 300 K.

3. Results and Discussions

3.1 Morphological and structural changes of nanoparticles prepared from various starting materials

Fig. 1 shows TEM images of α-FeOOH as a starting material, α-Fe produced by the reduction of α-FeOOH, and α”-$Fe_{16}N_2$ formed by the nitriding of α-Fe. The shape of the Fe hydroxide particles is spindle-like. Reduction was performed in an atmosphere of flowing H_2 at 380 °C for 4 h, and produced aggregates of nanoparticles by sintering. Subsequent nitriding was performed in an atmosphere of flowing NH_3 at 160 °C for 8 h. No morphological differences were observed between the reduced α-Fe and nitrided α”-$Fe_{16}N_2$ nanoparticle assemblies.

Fig. 2 shows TEM images of the ɤ-Fe_2O_3 starting material, α-Fe reduced from ɤ-Fe_2O_3 and α”-$Fe_{16}N_2$ as the nitriding product from α-Fe. The shape of the ɤ-Fe_2O_3 particles is spherical. Reduction was conducted in an atmosphere of flowing H_2 at 300 °C for 4 h. The reduction process caused the nanoparticles to form aggregates by sintering, as with the α-FeOOH starting material. Nitriding was performed in an atmosphere of flowing NH_3 at 145 °C for 8 h. The nitriding process did not result in any morphological changes, in the same way that no changes were observed with the α-FeOOH starting material.

Fig. 3 shows TEM images of the Fe_3O_4 starting material, α-Fe reduced from Fe_3O_4, and α”-$Fe_{16}N_2$ by the nitriding of α-Fe. The shape of the Fe_3O_4 particles is cubic. Reduction was performed in an atmosphere of flowing H_2 at 340 °C for 4 h. The reduction and nitriding processes did not generate any obvious macroscopic morphological changes, in contrast to that observed with the α-FeOOH and ɤ-Fe_2O_3 starting materials.

Fig. 4 shows representative XRD patterns of the α”-$Fe_{16}N_2$ nanoparticles produced from various starting materials. In the case of α”-$Fe_{16}N_2$ nanoparticles produced from α-FeOOH, ɤ-Fe_2O_3, all X-ray diffracted

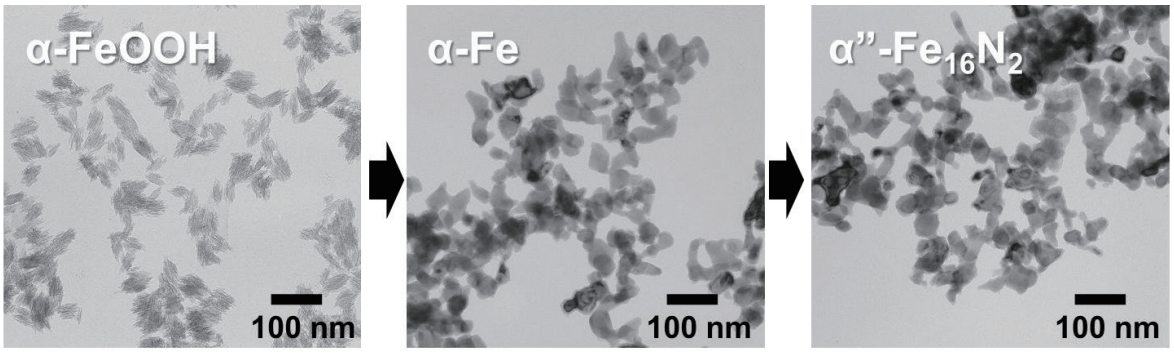

Fig.1 TEM images of α-Fe and α”-$Fe_{16}N_2$ produced from α-FeOOH as a starting material.

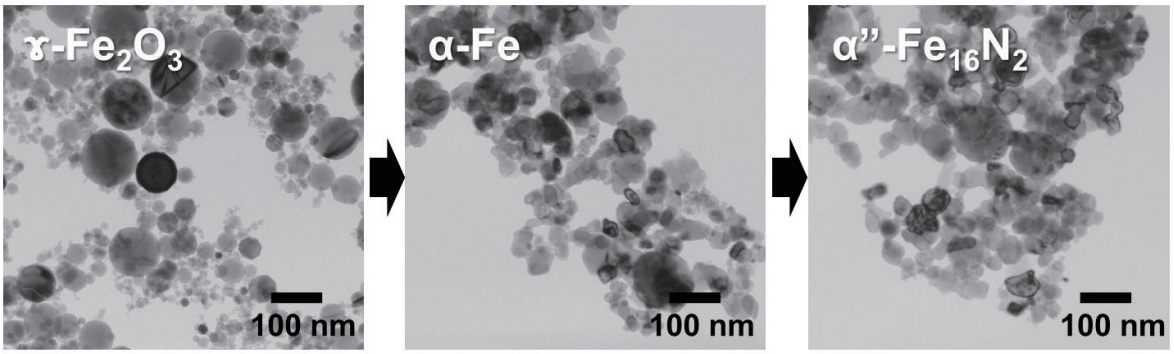

Fig. 2 TEM images of α-Fe and α”-$Fe_{16}N_2$ produced from ɤ-Fe_2O_3 as a starting material.

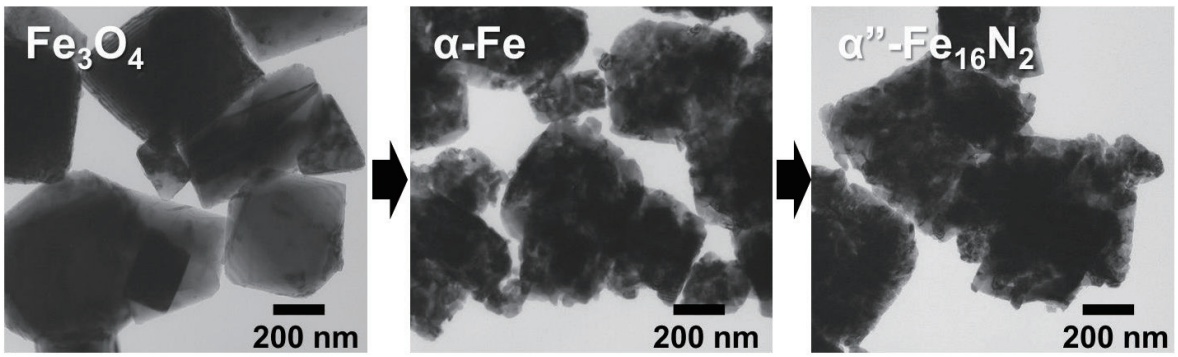

Fig. 3 TEM images of α-Fe and α”-$Fe_{16}N_2$ produced from Fe_3O_4 as a starting material.

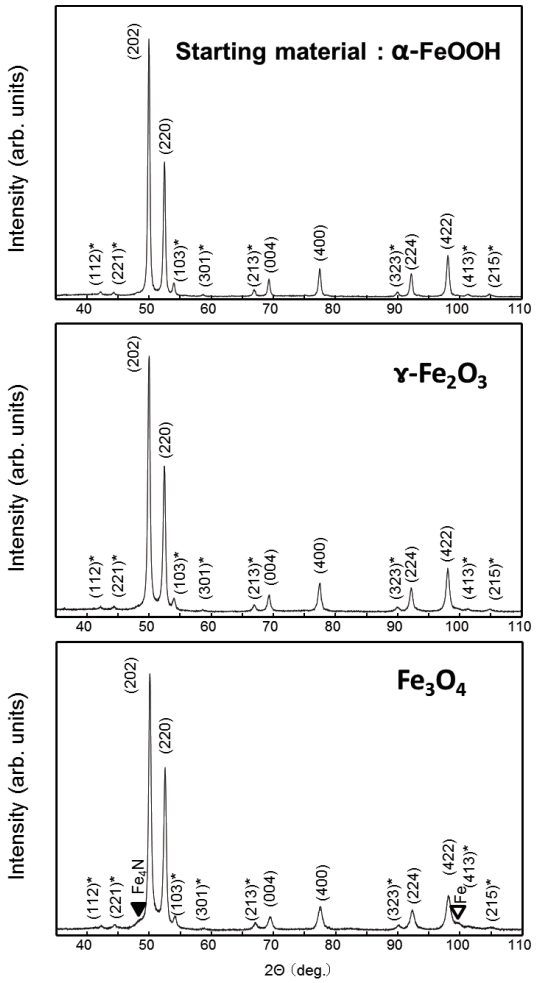

Fig. 4 XRD patterns of the α"-$Fe_{16}N_2$ nanoparticles produced from various starting materials. Asterisks show super-lattice diffraction of N ordered site.

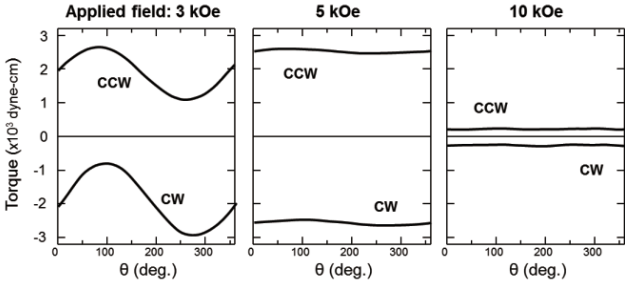

Fig. 5 Torque loss curves of α"-$Fe_{16}N_2$ randomly oriented particle assemblies produced from α-FeOOH changing applying field. CW indicates clockwise rotation and CCW indicates counter-clockwise rotation.

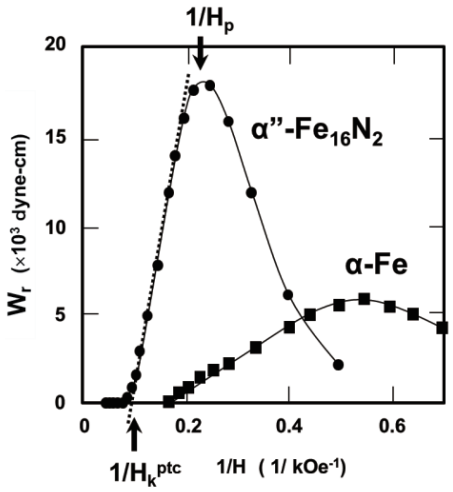

Fig. 6 Rotational hysteresis loss curves of α-Fe and α"-$Fe_{16}N_2$ nanoparticles assemblies produced from α-FeOOH.

line were identified as α"-$Fe_{16}N_2$. On the other hand, very small diffracted line besides diffractions of α"-$Fe_{16}N_2$ observed at diffraction angles around 48 and 99 degrees for α"-$Fe_{16}N_2$ nanoparticles produced from Fe_3O_4. It is supposed that these additional diffracted line correspond Fe_4N and α-Fe, respectively.

3.2 Shape anisotropy with respect to the agglomeration of nanoparticles

Fig. 5 shows the torque loss curves of α"-$Fe_{16}N_2$ randomly oriented particle assemblies produced from α-FeOOH changing applying field from 3 to 10 kOe. Rotational hysteresis loss W_r is measured as the region of enclosed area by these clockwise and counterclockwise torque curves. In the case of applying magnetic field H is larger than the half of anisotropy field H_k and smaller than H_k for the randomly oriented particles, rotational hysteresis loss W_r is observed and W_r changes as a function of magnetic field[9]. Fig. 6 shows rotational hysteresis loss curves of α-Fe and α"-$Fe_{16}N_2$ nanoparticles assemblies produced from α-FeOOH. H_k^{ptc} was defined by plotting W_r versus inverse applied field and finding the intercept by linearly extrapolating to zero hysteresis loss. H_p is the magnetic field where W_r reaches its maximum which corresponds to the switching field of assemblies of nanoparticles. H_k^{ptc} and H_p were evaluated with applying magnetic field up to 15 kOe. In the case of assemblies of particles which were magnetically isolated ideally, the value of magnetic field where W_r vanishes is independent of particle alignment (crystallographic orientation) and corresponds to H_k^{ptc}. Similar rotational hysteresis loss analysis had been already applied to the thin film recording media[10,11].

Table 1 shows the magnetic properties of α-Fe and α"-$Fe_{16}N_2$ nanoparticle assemblies produced from the different starting materials, as measured with the VSM and torque magnetometer. M_s for the α-Fe nanoparticle assemblies ranged from 205 to 198 emu/g according to the starting material. Compared to the literature value of the magnetization 218 emu/g for α-Fe, these values are lower from 6 to 9 % than the literature value. It is assumed that oxidation of surface of the α-Fe nanoparticles may cause this decrease in magnetization. H_c for the α-Fe nanoparticle assemblies ranged from 0.8 to 0.3 kOe according to the starting material, and H_k^{ptc}

Table 1. Magnetic properties of α-Fe and α"-$Fe_{16}N_2$ nanoparticle assemblies produced from various starting materials.

	α-Fe			α"-$Fe_{16}N_2$		
Starting material	α-FeOOH	ɤ-Fe_2O_3	Fe_3O_4	α-FeOOH	ɤ-Fe_2O_3	Fe_3O_4
M_s (emu/g)	205	203	198	226	192	180
H_c (kOe)	0.8	0.6	0.3	2.2	1.9	1.1
H_p (kOe)	2.0	1.7	1.3	4.2	3.8	3.0
H_k^{ptc} (kOe)	5.4	6.8	7.2	12.0	11.0	11.3
ΔN^{ptc}	3.3	4.3	4.6	——	——	——
Aspect ratio * - ellipsoid -	2.2	3.0	3.5	——	——	——

* Equivalent aspect ratio as nanoparticle assemblies

for the α-Fe nanoparticle assemblies also ranged from 5.4 to 7.2 kOe. For α-Fe nanoparticle assemblies, the anisotropy field H_k^{ptc} is considered to be due to the shape anisotropy of the nanoparticle assemblies because the magnetocrystalline anisotropy constant K_1 for α-Fe with cubic symmetry is too small (ca. 1×10^5 erg/cm^3). It is considered that the differences of H_k^{ptc} are derived from the difference of shape anisotropy in the assemblies of α-Fe nanoparticles that are formed during the reduction process. H_c for the α-Fe nanoparticle assemblies decreased from 0.8 to 0.3 kOe even though H_k^{ptc} of them increased from 5.4 to 7.2 kOe. It is assumed that H_c is not determined by only shape anisotropy. Further detailed investigation is necessary to reveal the factor which affects H_c of α-Fe.

Shape anisotropy is expressed as $K_u^{shape} = \Delta N \cdot M_s^2/2$ (or $H_k^{shape}=\Delta N \cdot M_s$). ΔN is the difference of the demagnetization coefficients between the long and short axes of a particle. The experimentally determined H_k^{ptc} was used to estimate ΔN^{ptc} as an equivalent demagnetization coefficients as nanoparticle assemblies. Fig. 7 shows an example of the calculated result[12] for

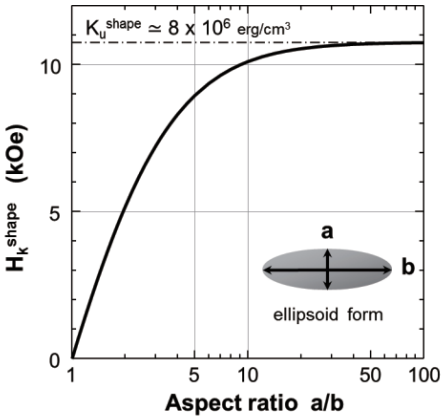

Fig. 7 Shape anisotropy field as a function of the aspect ratio for the ellipsoid form.

H_k^{shape} as a function of the aspect ratio, assuming an ellipsoid form and that the M_s of α-Fe is 218 emu/g. In this way, the values of ΔN^{ptc} were determined to range from 3.3 to 4.6 for the corresponding aspect ratios of α-Fe nanoparticle assemblies estimated with this scheme, from 2.2 to 3.5. As shown in Fig. 7, the maximum shape anisotropy is expected to be 8×10^6 erg/cm^3 with a high aspect ratio of more than 50 which is considered to be very difficult to realize.

On the other hand, H_c for the α"-$Fe_{16}N_2$ nanoparticle assemblies ranged from 2.2 to 1.1 kOe for different starting materials. The reason why that H_c of α"-$Fe_{16}N_2$ nanoparticles which were produced from Fe_3O_4 is lower than those of α"-$Fe_{16}N_2$ nanoparticles which were produced from α-FeOOH and ɤ-Fe_2O_3 is considered due to the additional α-Fe which was observed in X-ray diffraction(Fig. 4). H_k^{ptc} for the α"-$Fe_{16}N_2$ nanoparticle assemblies were not significantly different, ranging from 11 to 12 kOe. The magnetocrystalline anisotropy field H_k^{int} of α"-$Fe_{16}N_2$ determined for a pseudo single -crystalline film was 11.2 kOe[13]. This H_k^{ptc} for the α"-$Fe_{16}N_2$ nanoparticle assemblies are almost equal to H_k^{int}. If we assume α"-$Fe_{16}N_2$ nanoparticle assemblies have the same magnetocrystalline anisotropy field H_k^{int} of a pseudo single-crystalline film, the shape anisotropy is considered to be very small in α"-$Fe_{16}N_2$ nanoparticle assemblies.

3.3 Evaluation of magnetic interaction among α"-$Fe_{16}N_2$ nanoparticle assemblies

Fig. 8 shows plots of the normalized coercive force (H_c/H_k^{ptc}) versus normalized switching field (H_p/H_k^{ptc}) for α"-$Fe_{16}N_2$ nanoparticle assemblies produced from the various starting materials. H_c/H_k^{ptc} varied from 0.10 to 0.26 and H_p/H_k^{ptc} varied from 0.26 to 0.35. In the ideal magnetization reversal mode due to the coherent rotation of the magnetic moment with nonmagnetic interaction (Stoner-Wohlfarth type)[14] , H_c/H_k^{ptc} is equal to 0.48 and H_p/H_k^{ptc} is equal to 0.51. According to the micromagnetic simulation, and it was demonstrated

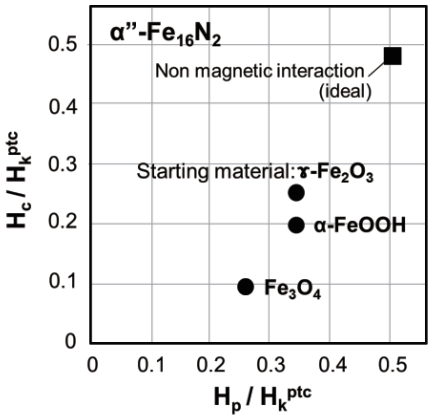

Fig. 8 Plots of H_c/H_k^{ptc} and H_p/H_k^{ptc} for α"-$Fe_{16}N_2$ nanoparticles prepared from various starting materials.

that both H_c and H_p decrease with increasing magnetic interaction among grains in thin film media[11]. Compared to the ideal values of H_c/H_k^{ptc} and H_p/H_k^{ptc}, these values of α"-$Fe_{16}N_2$ nanoparticles prepared from various starting materials are relatively small. To increase the coercivity of α"-$Fe_{16}N_2$ nanoparticles, it is necessary to decrease magnetic interaction.

3.4 Toward an increase in the coercivity of α"-$Fe_{16}N_2$ nanoparticle assemblies

The empirical figure known as the magnetic hardness parameter $\kappa = (K_1/\mu_0 M_s^2)^{1/2}$ is a useful parameter to consider how to approach the construction of modern permanent magnet[15]. The κ value for $Nd_2Fe_{14}B$ as a typical modern magnet, is 1.54, while that for α"-$Fe_{16}N_2$ is 0.53. It is recommended that κ be greater than 1, which corresponds to a value of $K_1 \simeq 3\times10^7$ erg/cm^3, assuming the same magnetization of $Nd_2Fe_{14}B$, 165 emu/g. The expected shape anisotropy is in the order of 10^6 erg/cm^3 for α"-$Fe_{16}N_2$ nanoparticles even though a high aspect ratio is realized (Fig. 7); therefor, magnetocrystalline anisotropy in the order of 10^7 erg/cm^3 is still required, in addition to improvement of the magnetic isolation among nanoparticles, for application as a permanent magnets.

4. Conclusion

The structural and magnetic properties of α"-$Fe_{16}N_2$ nanoparticles synthesized from different starting materials were examined, and the magnetic anisotropy of nanoparticle assemblies and magnetic interactions among nanoparticles were evaluated by rotational hysteresis loss analysis.

1. α-Fe nanoparticle assemblies produced by reduction and nitriding of different starting materials show exhibited different values of H_k^{ptc} ranging from 5.4 to 7.2 kOe. It is considered that the differences of H_k^{ptc} are derived from the difference of shape anisotropy in the assemblies of α-Fe nanoparticles that are formed during the reduction process. From these H_k^{ptc} values, the aspect ratio of α-Fe nanoparticle assemblies were estimated to be in the range of 2.2−3.5.

2. H_c for the α"-$Fe_{16}N_2$ nanoparticle assemblies ranged 2.2 to 1.1 kOe for different starting materials. H_k^{ptc} for the α"-$Fe_{16}N_2$ nanoparticle assemblies were not significantly different, ranging from 11 to 12 kOe.

3. The normalized coercive force (H_c/H_k^{ptc}) and normalized switching field (H_p/H_k^{ptc}) are 0.10−0.26 and 0.26−0.35 respectively, which indicates large magnetic interactions.

4. As the expected shape anisotropy is in the order of 10^6 erg/cm^3 for α"-$Fe_{16}N_2$ nanoparticles even though a high aspect ratio is realized, magnetocrystalline anisotropy on the order of 10^7 erg/cm^3 is still required, in addition to improvement of the magnetic isolation among nanoparticles to realize a permanent magnet.

Acknowledgements This work was partially supported by the New Energy and Industrial Technology Development Organization (NEDO), the Matching Planner Program from the Japan Science and Technology Agency (JST) and the Technology Research Association of Magnetic Materials for High-Efficiency Motors (MagHEM).

References

1) T. K. Kim, M. Takahashi: *Appl. Phys. Lett.*, **20**, 492 (1972)
2) J. M. D. Coey, K. O'Donnell, Q. Qinian, E. Touchais, K. H. Jack: *J. Phys.: Condens. Matter*, **6**, L23 (1994).
3) M. Komuro, Y. Kozono, M. Hanazono, and Y. Sugita: *J. Appl. Phys*, **67**, 5126 (1990)
4) M. Takahashi, H. Shoji, H. Takahashi, T. Wakiyama: *IEEE Trans. Magn.*, **29**, 3040 (1993).
5) M. Takahashi, H. Shoji: *J. Magn. Magn. Mater.* **208**, 145 (2000).
6) E. Kita, K. Shibata, H. Yanagihara, Y. Sasaki, M. Kishimoto: *J. Magn. Magn. Mater.*, **310**, 2411 (2007).
7) S. Kikkawa, A. Yamada, Y. Masubuchi, T. Takeda: *Mater. Res. Bull.*, **43**, 3352 (2008).
8) T. Ogawa, Y. Ogata, R Gallage, N. Kobayashi, N Hayashi, Y Kusano, S. Yamamoto, K. Kohara, M. Doi, M. Takano, M Takahashi: *Appl. Phys. Expres*s, **6**, 073007 (2013).
9) I. S. Jacobs, F. E. Luborsky: *J. Appl. Phys.*, **28**, 467 (1957).
10) M. Takahashi, T. Shimatsu, M. Suekane, M. Miyamura, K. Yamaguchi, H. Yamasaki: *IEEE Trans. Magn.*, **28**, 3285 (1992).
11) I. A. Beardsley and V.S. Speriosu: *IEEE Trans. Magn.*, **26**, 2718 (1990).
12) R. C. O'Handley, *Modern Magnetic Materials: Principle and Applications,* 1st ed. (John Wiley & Sons, Inc., New York, 1999), pp.38-43.
13) M. Takahashi, Y. Takahashi, K. Sunaga, H. Shoji: *J. Magn. Magn. Mater.*, **239**, 479 (2002).
14) E. C. Stoner, E. P. A. Wohlfarth: *Phil. Trans. R. Soc. Lond.*, **A 240**, 599 (1948).
15) R. Skomski, J. M. D. Coey: *Scripta Materialia*, **112**, 3 (2016)

Received Sep. 28, 2016; Revised Dec. 19, 2016; Accepted Mar. 08, 2017

J. Magn. Soc. Jpn., **41**, 63-65 (2017)

Letter

Temperature Characteristics of the Dynamic Magnetic Loss of Ferrite

H. Saotome, K. Azuma and Y. Hamamoto

Faculty of Engineering, Chiba University, *1-33 Yayoi-cho, Inage-ku, Chiba 263-8522, Japan*

The dynamic magnetic loss in ferrites is obtained by subtracting the hysteresis loss, which is independent of the excitation frequency, from the iron loss. In the high frequency excitation region, the dynamic magnetic loss is the dominant component of the iron loss in ferrites. The iron loss in ferrite is temperature-dependent and this dependence has been described in product catalogs, where the hysteresis and dynamic losses are not separated. The catalog data are measured using sinusoidal wave voltage excitation, whereas ferrite cores are commonly used under rectangular wave voltage excitation in DC-DC converters. In this paper, the experimentally obtained temperature characteristics of the hysteresis and dynamic magnetic losses for rectangular wave voltage excitation are shown separately, and it is found that the two are different. This suggests that the physical mechanisms involved are different as well. Thus, it is important to consider the temperature characteristics of the dynamic magnetic loss to produce low-loss ferrites.

Key words: ferrite, Mn-Zn, iron loss, dynamic magnetic loss, *B-H* loop, temperature

1. Introduction

Ferrite cores are mainly used in DC-DC converters, where their switching frequencies are typically around 100 kHz. The eddy current loss in ferrites is negligible, even when they are excited at such high frequencies, because of the very high resistivity of grain boundaries. Thus, the power loss of ferrites is considered to be the magnetic loss. For a given magnetic induction maximum, B_m, the power loss of ferrites depends on the temperature. This dependence has been described in a product catalog, where the excitation voltage waveform used was sinusoidal [1].

The magnetic loss in ferrites consists of hysteresis and dynamic magnetic losses [2]. The area of the *B-H* loop varies with the exciting frequency, i.e., the time derivative of the magnetic induction, dB/dt. The hysteresis loss (J/m^3) is defined as the minimum *B-H* loop area with respect to the exciting frequency when B_m is kept constant, as shown by the broken line in Fig. 1. When the excitation frequency, or dB/dt, is increased, the *B-H* loop widens, as depicted by the solid line in Fig. 1. The dynamic magnetic loss (J/m^3) is defined by the gray area in the figure.

Although it is of great interest to investigate the generation mechanism of the magnetic losses, this is not easy. To determine whether the hysteresis and dynamic magnetic losses are generated by the same mechanism, the present authors measured the temperature behavior of both quantities in a previous study [3]. We found no significant difference of the dynamic magnetic loss between at 0 °C and at room temperature. In that study [3], we used TDK PC40 Mn-Zn ferrite, whereas here, we used TDK PC47, whose power loss temperature dependence is approximately 1.8 times stronger than that of PC40 [1]. The dimensions of the core used in the experiments is shown in Fig. 2. The power loss measurements were carried out at 0 °C and 30 – 70 °C.

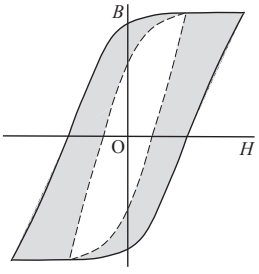

Fig. 1 *B-H* loop.

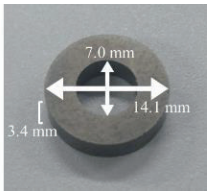

Fig. 2 Toroidal core used in experiments.

2. Instrumentation

In order to set the temperature of the ferrite core to 0 °C and 30 – 70 °C, the temperature control setups shown in Figs. 3(a) and 3(b), respectively, were prepared. The core was completely submerged in distilled water in both cases. In Figs. 3(a) and 3(b), the distilled water was surrounded by ice and a thermal insulator, respectively. In Fig. 3(b), the water temperature was controlled with a power source, heater, and thermocouple. The duration of the excitation was short enough to keep the rise in core temperature below 1 °C.

The product catalog for PC47 shows the temperature characteristics of the core loss under sinusoidal waveform voltage excitation at 100 kHz and B_m = 200 (mT). The measurement results obtained in the range of 30 °C to 70 °C using the present setup coincide with the

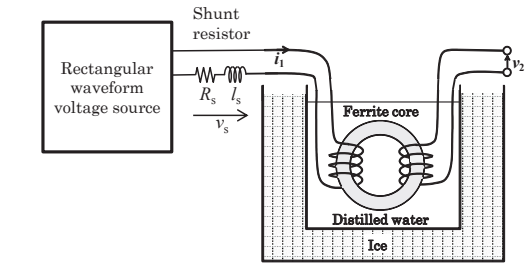

(a) At roughly 0 °C

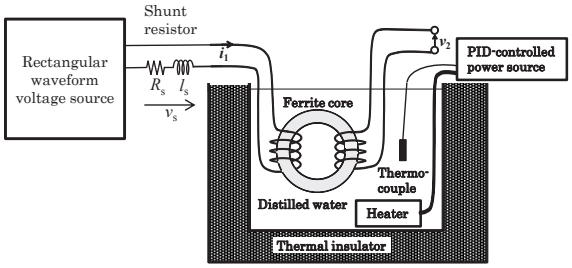

(b) Above 30 °C

Fig. 3 Measurement setups.

catalog data under the same conditions.

In this study, the ferrite core was excited by a rectangular waveform voltage, i.e., at constant dB/dt, because we wanted to measure the power loss of the ferrite with respect to the parameter dB/dt. The rectangular waveform voltage sources shown in Figs. 3(a) and 3(b) consisted of a function generator and an amplifier, or an FET inverter. The amplifier and FET inverter were used to generate dB/dt smaller and larger than 200 mT/μs, respectively.

To measure the excitation current, i_1, a shunt resistor with a known stray inductance was used. The i_1 waveform was calculated by using the shunt resistor voltage, v_s, and the compensation for the deviation due to the stray inductance. *B-H* loops are obtained with i_1, the time integral of the search-coil-induced voltage, v_2, and the core dimensions. When the excitation current is too large, v_2 deviates from the rectangular waveform due to v_s. In such cases, the output waveform of the function generator is adjusted to compensate for the distortion [3].

3. Measurement results

Six *B-H* loops measured at 0 °C and 70 °C are shown in Figs. 4(a) and 4(b), respectively. They were obtained under rectangular waveform voltage excitation with dB/dt = 1, 200, 400, 600, 800 and 1000 mT/μs. The smallest and largest *B-H* loops in the figures correspond to 1 and 1000 mT/μs, respectively. The maximum magnetic flux density, B_m, was kept at 200 mT for each *B-H* loop. Between 0 °C and 70 °C, the power loss of the ferrite decreases with increasing temperature. The hysteresis loss corresponding to the area of the smallest *B-H* loop in each figure also decreases. Moreover, the

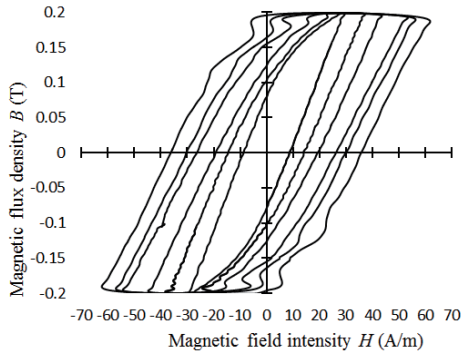

(a) 0 °C

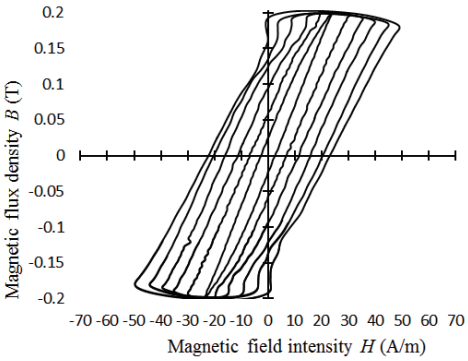

(b) 70 °C

Fig. 4 *B-H* loops (B_m = 200 mT).

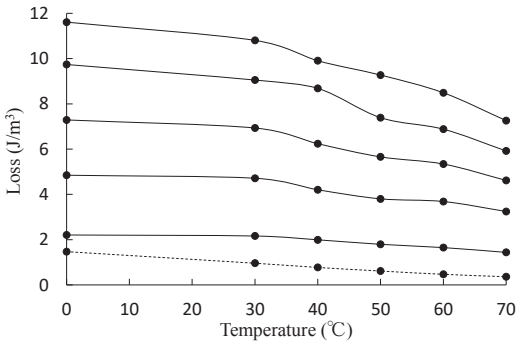

(a) B_m = 100 mT

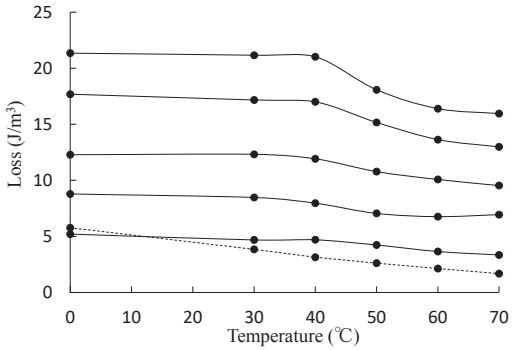

(b) B_m = 200 mT

Fig. 5 Temperature characteristics of the dynamic magnetic loss with dB/dt = 1000, 800, 600, 400 and 200 mT/μs from the top down, respectively. The bottom broken lines show the hysteresis losses.

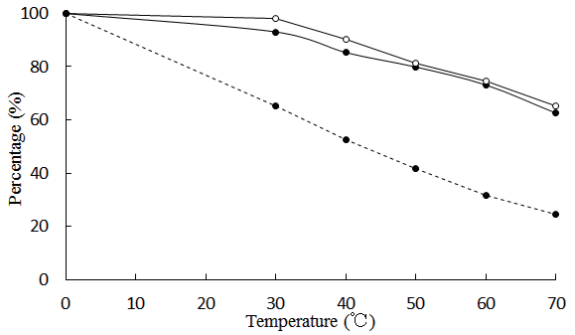

(a) B_m = 100 mT

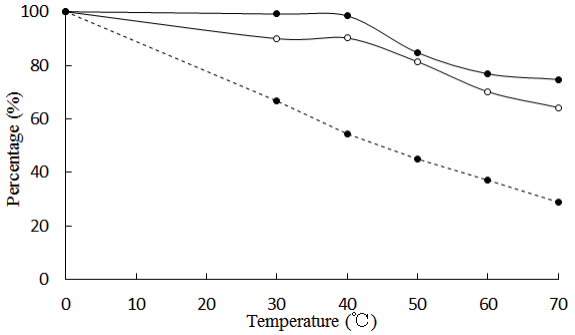

(b) B_m = 200 mT

Fig. 6 Temperature characteristics of the dynamic magnetic loss: normalized values with respect to the values at 0 °C for dB/dt = 1000 (●) and 200 (○) mT/μs. The bottom broken lines show the hysteresis losses normalized to the values at 0 °C.

dynamic magnetic loss decreases slightly. In Fig. 4, the magnetic field intensities fluctuate a little near $\pm B_m$, i.e., the exciting current oscillates slightly when the rectangular waveform voltage changes its polarity very quickly. The fluctuation is caused by the stray capacitance of the winding. However, it does not influence the B-H loop areas, because the energy stored in the stray capacitance does not affect the area in a period. The capacitance energy is restored to the voltage source.

Similar to the experiments resulting in Fig. 4, B-H loops were also measured at 30, 40, 50, 60 and 70 °C. The temperature characteristics of the hysteresis and dynamic magnetic losses are shown in Figs. 5(a) and 5(b), where B_m is kept at 100 mT and 200 mT, respectively. The measured dynamic magnetic losses are plotted with dB/dt = 1000, 800, 600, 400 and 200 mT/μs from the top down, respectively, and the bottommost broken lines represent the hysteresis losses. The dynamic magnetic loss becomes larger than the hysteresis loss and dominates with increasing dB/dt, regardless of the temperature. To investigate whether the difference in temperature characteristics between the hysteresis and dynamic magnetic losses can be clarified, the normalized values were re-plotted (see Fig. 6), with 100 % representing the values at 0 °C for each of the losses. Figures 6(a) and 6(b) revealed that between 0 °C and 30 °C, the hysteresis loss decreased with temperature more steeply than the dynamic magnetic loss; the normalized hysteresis loss curves in Figs. 6(a) and 6(b) almost coincide. Thus, the temperature characteristics of the hysteresis and dynamic magnetic losses are different, which suggests that, microscopically, their generation mechanisms are not precisely the same.

4. Conclusions

The hypothesis that the dynamic magnetic loss corresponds to the eddy current loss in ferrite grains has been disproved [4]. Thus, the dynamic magnetic loss must be caused by a magnetic phenomenon explainable by electron spins, as in the case of the hysteresis loss, whereas the eddy current can be explained by free electron motion. However, the experimental results presented here suggest that the generation mechanism of the dynamic magnetic loss cannot be exactly the same as that of the hysteresis loss, given the difference in their temperature characteristics.

The hysteresis losses, normalized to the values at 0 °C, decrease with temperature to a greater extent than the normalized dynamic losses. On the other hand, the temperature dependence of the dynamic magnetic loss in the raw data is stronger than that of the hysteresis loss. The dynamic magnetic loss is more dominant under large dB/dt conditions. Thus, ferrite manufacturers need to observe closely the temperature characteristics of the dynamic magnetic loss, rather than evaluating only the total magnetic loss.

References

1) *http://product.tdk.com/ja/catalog/datasheets/ferrite_mn-zn_material_characteristics_ja.pdf*
2) H. Saotome and Y. Sakaki: *IEEE Trans. Magn.*, **33**, 728 (1997)
3) H. Saotome and H. Ohta: *J. Magn. Soc. Jpn.* **39**, 62(2015)
4) H. Saotome: *J. Magn. Soc. Jpn.* **40**, 19(2016)

Received Feb. 15, 2017; Accepted Mar. 27, 2017

J. Magn. Soc. Jpn., **41**, 66-69 (2017)

Letter

Effect of Amorphous Region on Magnetic Orientation of Poly(lactic acid) Blend Films with Different Molecular Weight

Rei Nakayama, Hiroki Ikake*, Kimio Kurita*, Shigeru Shimizu*, Satoshi Kurumi*, Kaoru Suzuki*, Kohki Takahashi** and Hiroyuki Nojiri**

Graduate School of Science and Technology, Nihon Univ., *1-8-14 Kanda Surugadai, Chiyoda-ku, Tokyo 101-8308, Japan*
*College of Science and Technology, Nihon Univ., *1-8-14 Kanda Surugadai, Chiyoda-ku, Tokyo 101-8308, Japan*
** Institute for Materials Research, Tohoku Univ., *2-1-1 Katahira, Aobaku, Sendai, Miyagi, Japan*

The magnetic-field-induced blend films, poly(L-lactide)(PLLA10) (M_n = 1.0 × 10^5) and poly(DL-lactide) (M_w = 1.0 × 10^4 (PDLLA1) and 1.0 × 10^5 (PDLLA10)) were prepared in isothermal process under the magnetic-field 10 T. The effects of amorphous region, i.e., molecular weight of PDLLA effect on crystallization and orientation of PLLA in the films were investigated using wide-angle X-ray diffraction and polarizing microscopy. The crystallinity of each films showed 60% at crystallization growth time t_c = 30 hrs irrespective of PDLLA molecular weight. The degree of orientation of PLLA10/PDLLA10 film increased with increasing t_c. We concluded that the blending with amorphous high-molecular-weigh PDLLA and crystallization in an applied high magnetic field is effective to achieve the PLLA film that has higher crystallinity and orientation.

Key words: magnetic-induced-orientation film, poly(L-lactide), poly(DL-lactide), amorphous, blend film, high magnetic field

1. Introduction

Recently, biomass plastics are interest for saving petroleum resources and reduction of carbon dioxide. It is especially expected that the biomass plastics produced from plant-derived raw materials. For example, poly(lactic acid)(PLA) is well-known biomass plastic which are produced from renewable resources and used in many field such as biomedical, packaging and ecological fields.

There has been an extensive effort to investigate for PLA such as crystal structure, crystal growth, melting behavior, and applications.[1] Many researchers have studied stereocomplex consist of blend of PLLA and poly(D-lactic acid)(PDLA) as a solution to improve the thermal and physical properties of PLLA.[2) 3)] However, PDLA is the high cost as industrial raw material. Another approach such as the orientation control is proposed to improve the properties of PLLA. Orientation control of PLLA is an important subject because the physical properties of PLLA are strongly affected by the orientation. By using mechanical orientation, one obtains materials with ordered polymer crystals. This method is often used in industry, however there is a fear of deformation. PLLA is known to be miscible with PDLLA and develop PLLA crystal in PDLLA.[4) 5)] We previously reported that the magnetic-induced oriented films of PLLA/PDLLA, which PDLLA has lower molecular weight than that of PLLA.[6)]
Crystallization of PLLA has been developed in PDLLA and shown the high degree of orientation.

In this work, the influence of molecular weight of amorphous PDLLA in the PLLA/PDLLA blend films on the crystallization and orientation behaviors of PLLA was investigated.

2. Experimental

2.1 Materials

PLLA of M_n = 1.0 × 10^5 (PLLA10), and PDLLA of M_w = 1.0 × 10^4 (PDLLA1) and M_w = 1.0 × 10^5 (PDLLA10) were purchased from Sigma-Aldrich Co. The optical purity was determined by the specific optical rotation measurement of PLA sample $[\alpha]_{sample}$ using P-2300 polarimeter (JASCO Corporation, Japan) with a wavelength of 589.3 nm (D-line of the sodium lamp) at 25 °C.

$$OP\% = \frac{[\alpha]_{sample}}{[\alpha]_{PLLA}} \times 100 \qquad (1)$$

where $[\alpha]_{PLLA}$ is the specific rotation of PLLA with 100% of L stereoisomer and value of -156° was used.[7)] The percentage optical purity of PLLA10, PDLLA1 and PDLLA10 were 98.3, 0.4 and 0.5%, respectively. This result shows both PDLLA10 and PDLLA1 are consisting of racemic lactate units and are completely noncrystallizable polymers.

2.2 Preparation of PLLA/PDLLA solution-cast films

Two kinds of solution-cast blend films, PLLA10/PDLLA1 film and PLLA10/PDLLA10 film, were prepared. Concentration of 10 wt% of PLLA10 chloroform solution and 10 wt% of PDLLA1 or PDLLA10 chloroform solution were mixed and stirred for 2 hrs, and the solution was put in petri dish and was

stood for 24 hrs. PLLA/PDLLA films were dried at 70 °C for 2 hrs in vacuum oven. The thickness of each films was 100 ± 20μm.

2.3 Preparation of PLLA/PDLLA oriented films under high magnetic field

Preparation of PLLA/PDLLA oriented films in a magnetic field was carried out at Institute for Materials Research, Tohoku University. The temperature program for the crystallization of PLLA in the blend films was illustrated in Figure 1. The films were heated from room temperature to the annealing temperature 185°C at a rate of 3°C/min and held constant for 10 min. Then, films were cooled to 140°C (isothermal crystallization temperature) for isothermal crystallization time t_c = 0, 2, 15 and 30 hrs. The magnetic field of 10 T was applied throughout the whole thermal process.

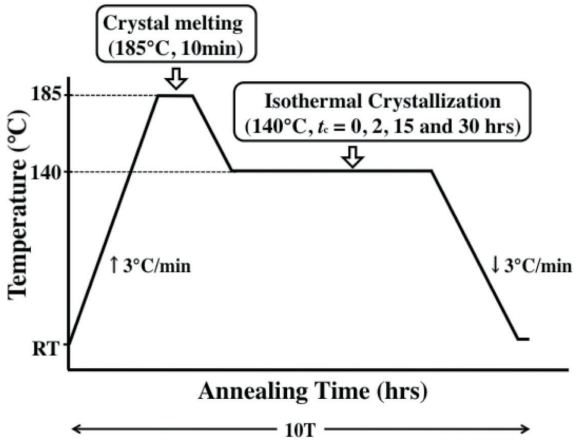

Fig.1 Thermal process for PLLA10/PDLLA1 and PLLA10/PDLLA10 films. Throughout the whole thermal process, the magnetic field of 10 T was applied.

2.4 Measurements

WAXD measurement was carried out using X'Pert PRO MPD(PANalytical, Japan) operated at 45 kV and 40 mA to generate Ni-filtered CuKα X-ray beam. Scanning speed was 0.01°/s and measurement range was 3 – 60° at room temperature. Crystals growth in the films was observed by polarization microscope (BX53-33P-OC-1, Olympus, Japan).

3. Results and discussion

3.1 Crystallization of oriented films

In Figures 2 and 3, WAXD pattern of PLLA10/PDLLA1 and PLLA10/PDLLA10 films after annealing at 140°C for different periods was shown. PLLA shows the two dominant diffraction peaks at 16.7° and 19.1° of α-form crystal. These diffraction peaks are assigned to the 110/200 and 203 reflections, respectively. [8) 9) 10)] The intensity of these diffraction peaks increased gradually with increasing crystallization time. However, refraction peaks of 110/200 and 203 of the PLLA10/PDLLA10 film for t_c = 2 hrs have been not detected.

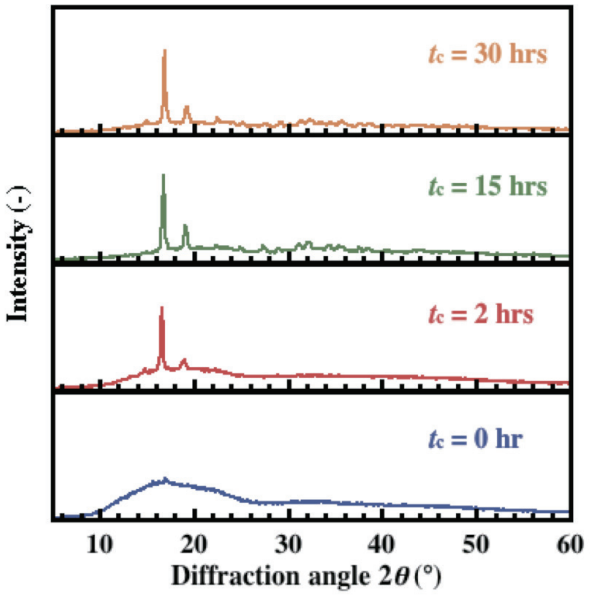

Fig.2 WAXD patterns of PLLA10/PDLLA1 films.

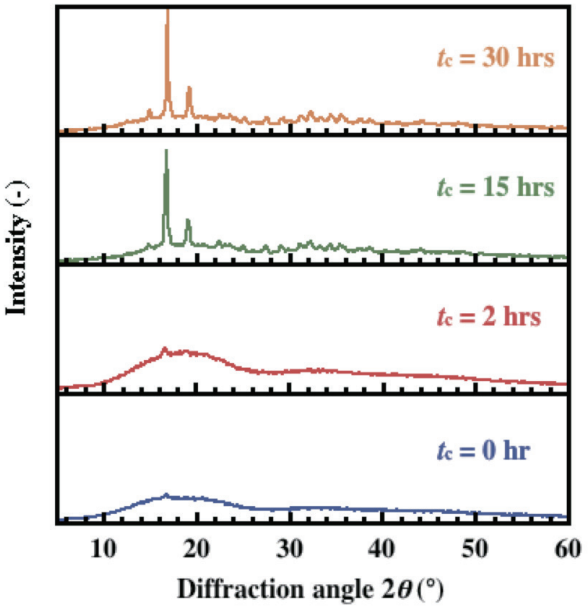

Fig.3 WAXD patterns of PLLA10/PDLLA10 films.

The relationship between t_c and the degree of crystallization X_c was shown in Figure 4. From the peak areas of WAXD patterns, X_c was calculated by the following equation,

$$X_C\% = \frac{S_{PLLA}}{S_{PLLA} + S_{PDLLA}} \times 100 \qquad (2)$$

where S_{PLLA} and S_{PDLLA} are PLLA and PDLLA

diffraction peaks areas.[11] X_c of neat PLLA film which prepared in the same condition also was shown for comparison. From the figure, it is clear that the induction period of PLLA crystallization of blend films are longer than that of neat PLLA10 film. The induction period of PLLA10/PDLLA1 is short in comparison with PLLA10/PDLLA10. This could be interpreted that the mobility of PLLA10 chains are large because the melt viscosity of low-molecular-weight PDLLA1 are lower than that of PDLLA10. The crystallization rate of both blend films is faster than that of neat PLLA after the induction period. The value of X_c of all films, however, attained about 60% for t_c = 30 hrs.

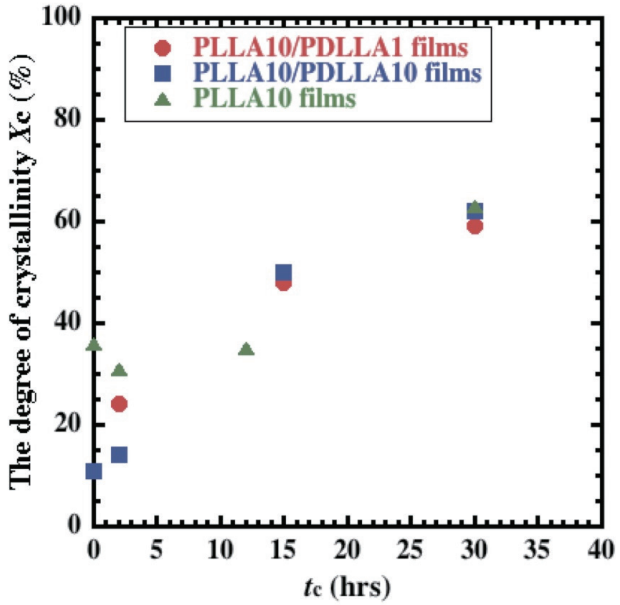

Fig. 4 The degree of crystallinity X_c by WAXD measurement of PLLA10/PDLLA1 and PLLA10/PDLLA10 films.

3.2 Magnetic orientation of oriented films

The c-axis of PLLA crystal in the PLLA/PDLLA film was oriented in the parallel direction to the magnetic field.[6] The degree of orientation was defined as the azimuthal angle of reflected intensity of 110/200 planes. The degree of the magnetic-field-induced orientation f_c was calculated by the following equations,

$$\langle \cos^2 \varphi \rangle = \frac{\int_0^{\frac{\pi}{2}} I(\varphi) \cos^2 \varphi \sin \varphi d\varphi}{\int_0^{\frac{\pi}{2}} I(\varphi) \sin \varphi d\varphi} \quad (3)$$

$$f_c = \frac{3\langle \cos^2 \varphi \rangle - 1}{2} \quad (4)$$

where φ is the azimuthal angle and I(φ) is the azimuthal intensity. Figure 5 shows f_c against t_c of blend films and neat PLLA film.

In the case of PLLA10/PDLLA10 film, f_c increased with increasing t_c. In contrast, a f_c of PLLA10/PDLLA1 and neat PLLA films are constant for all range of t_c, i.e., this shows that applied magnetic field has no effect on the orientation of these films.

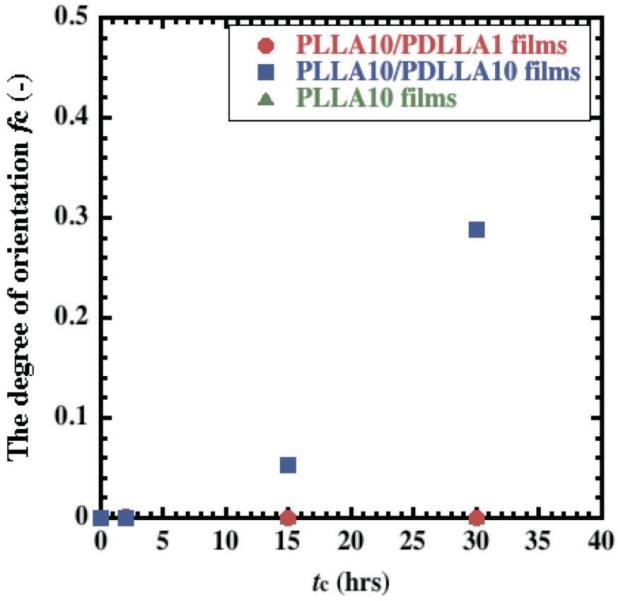

Fig. 5 The degree of orientation f_c by WAXD measurement of PLLA10/PDLLA1 and PLLA10/PDLLA10 films.

3.3 Isothermal crystalline behavior of oriented films

Figure 6 shows a polarizing optical micrograph of (A) PLLA10/PDLLA1, (B) PLLA10/PDLLA10, and (C) neat PLLA films. Optical micrographs were taken at different crystal growth time ranging from 0 to 30 hrs. These films show the formation of spherulite that was grown isothermally at 140°C, and its content increase with increasing t_c. As is seen in Figure 6(C), the spherulite radius of neat PLLA10 increased with

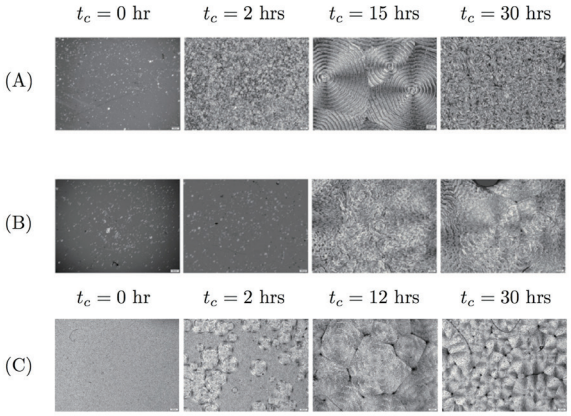

Fig.6 Polarized photomicrographs of films. (A): PLLA10/PDLLA1 and (B): PLLA10/PDLLA10 at t_c = 0, 2, 15 and 30 hrs. (C): neat PLLA10 at t_c = 0, 2, 12 and 30 hrs.

increasing t_c, and the behavior agrees with the literature.[12] On the other hand, the crystallization behavior of blend films could be explained by following.
Increasing of spherulites in both blend films is due to trapping amorphous PDLLA in the spherulite of PLLA.[5] [12] For t_c = 0 hr, the photomicrographs demonstrate small crystallites grew spherically from single nuclei. For t_c = 2 hrs, numbers of small crystallites increase in PLLA10/PDLLA1 film, but a faintly increase in PLLA10/PDLLA10 film. For t_c > 15 hrs, it is clear that the spherulites contents in each films increased with increasing crystal growth time. For t_c = 30 hrs, PLLA10/PDLLA1 film shows large optical textures in Figure 6(A).
Comparison with spherulite structure of PLLA10/PDLLA1 and PLLA10/PDLLA10, the latter is more disordered than the former. Formation of these large spherulites observed in PLLA10/PDLLA1 can be explained by the homogeneous crystallization. In contrast, PLLA10/PDLLA10 film shows small optical texture(Figure 6(B)). This is due to heterogeneous nucleation, i.e., the locally orientated domain.

4. Conclusions

We have investigated the magnetic-field-induced PLLA in amorphous PDLLA oriented films without nucleating agents in a 10 T magnetic field. The dependence of molecular weight of PDLLA on crystallization of PLLA in the blend films was not observed in the crystallization in the magnetic field. However, orientation behavior is quite different between PLLA10/PDLLA1 and PLLA10/PDLLA10 films. That is, trapping of low-molecular-weight PDLLA in the spherulite of PLLA10 show disturb the orientation of PLLA crystal. On the other hand, trapping high-molecular-weight PDLLA promote higher orientation film. Hence, the blending with amorphous high-molecular-weigh PDLLA and crystallization in an applied magnetic field is effective to achieve the PLLA film that has higher crystallinity and orientation.

References

1) R. Auras, L.-T. Lim, S. E. M. Selke, and H. Tsuji, Eds.: Poly(lactic acid) :*Synthesis, Structures, Properties, Processing, and Applications*, Wiley, New York, (2010).
2) Y. Ikada, K. Jamshidi, H. Tsuji, and S.-H. Hyon: *Macromolecules*, **20**, 906 (1987).
3) H. Tsuji, and Y. Ikada: *Polymer*, **40**, 6699 (1999).
4) H. Tsuji, and Y. Ikada: *J. Appl. Polym. Sci.*, **58**, 1793 (1995).
5) P. Pan, Z. Liang, B. Zhu, T. Dong, and Y. Inoue: *Macromolecules*, **42**, 3374 (2009).
6) R. Nakayama, H. Ikake, K. Kurita, S. Shimizu, S. Kurumi, K. Suzuki, K. Takahashi, and K. Watanabe: *Kobunshi Ronbunshu*, **72**, 661 (2015).
7) D. A. S. Marques, S. Jarmelo, C. M. S. G. Baptista, and M.H. Gil: *Macromol. Symp.*, **296**, 63 (2010).
8) W. Hoogsteen, A. R. Postema, A. J. Pennings, G. tenBrink, and P. Zugenmaier: *Macromolecules*, **23**, 634 (1990).
9) J. Zhang, Y. Duan, H. Sato, H. Tsuji, I. Noda, Sh. Yan, and Y. Ozaki: *Macromolecules*, **38**, 8012 (2005).
10) P. Pan, W. Kai, B. Zhu, T. Dong, and Y. Inoue: *Macromolecules*, **40**, 6898 (2007).
11) L. Bouapao, H. Tsuji, K. Tashiro, J. Zhang, M. Hanesaka: *Polymer*, **50**, 4007 (2009).
12) H. Tsuji, and Y. Ikada: *Polymer*, **37**, 595 (1996).

Received Dec. 08, 2016; Accepted Jan. 05, 2017

Editorial Committee Members・Paper Committee Members

Notice for Photocopying

編集委員・論文委員

複写をされる方へ

Journal of the Magnetics Society of Japan

Vol. 41 No. 3 (通巻第 291 号) 2017 年 5 月 1 日発行

Vol. 41 No. 3 Published May 1, 2017

by the Magnetics Society of Japan

Tokyo YWCA building Rm207, 1–8–11 Kanda surugadai, Chiyoda-ku, Tokyo 101–0062

Tel. +81–3–5281–0106 Fax. +81–3–5281–0107

Printed by JP Corporation Co., Ltd.

2–3–36, Minamikase, Saiwai-ku, Kanagawa 212–0055

Advertising agency: Kagaku Gijutsu-sha

発行：(公社)日本磁気学会 101–0062 東京都千代田区神田駿河台 1–8–11 東京YWCA会館 207 号室

製本：(株)ジェイピーコーポレーション 212–0055 神奈川県川崎市幸区南加瀬 2–3–36 Tel.（044）571–5815

広告取扱い：科学技術社 111–0052 東京都台東区柳橋 2–10–8 武田ビル 4F Tel.（03）5809–1132